



## Analysis of Electron Transparent Beam-Sensitive Samples Using Scanning Electron Microscopy Coupled with Energy-Dispersive X-ray Spectroscopy

Brostrøm, Anders; Kling, Kirsten Inga; Hougaard, Karin Sørig; Mølhave, Kristian

*Published in:*  
Microscopy and Microanalysis

*Link to article, DOI:*  
[10.1017/S1431927620001464](https://doi.org/10.1017/S1431927620001464)

*Publication date:*  
2020

*Document Version*  
Peer reviewed version

[Link back to DTU Orbit](#)

*Citation (APA):*  
Brostrøm, A., Kling, K. I., Hougaard, K. S., & Mølhave, K. (2020). Analysis of Electron Transparent Beam-Sensitive Samples Using Scanning Electron Microscopy Coupled with Energy-Dispersive X-ray Spectroscopy. *Microscopy and Microanalysis*, 26(3), 373-386. <https://doi.org/10.1017/S1431927620001464>

---

### General rights

Copyright and moral rights for the publications made accessible in the public portal are retained by the authors and/or other copyright owners and it is a condition of accessing publications that users recognise and abide by the legal requirements associated with these rights.

- Users may download and print one copy of any publication from the public portal for the purpose of private study or research.
- You may not further distribute the material or use it for any profit-making activity or commercial gain
- You may freely distribute the URL identifying the publication in the public portal

If you believe that this document breaches copyright please contact us providing details, and we will remove access to the work immediately and investigate your claim.

# Analysis of Electron Transparent Beam Sensitive Samples using Scanning Electron Microscopy coupled with Energy Dispersive X-ray Spectroscopy

Anders Brostrøm<sup>1,2</sup>, Kirsten Inga Kling<sup>1,3</sup>, Karin Sørig Hougaard<sup>2</sup>, and Kristian Mølhave<sup>1\*</sup>

<sup>1</sup>Technical University of Denmark, DTU Nanolab – National Centre for Nano Fabrication and Characterization, Fysikvej, Building 307, 2800 Kgs Lyngby, Denmark

<sup>2</sup>National Research Centre for the Working Environment, Lersø Parkallé 105, 2100 Copenhagen, Denmark

<sup>3</sup>SAXOCON A/S, Bredevej 2D, 2830 Virum, Denmark

\*Corresponding author: krmo@dtu.dk

## Abstract

Scanning electron microscopy, coupled with energy dispersive X-ray spectroscopy (EDS), is a powerful tool used in many scientific fields. It can provide nanoscale images, allowing size and morphology measurements, as well as provide information on the spatial distribution of elements in a sample. This study compares the capabilities of a traditional EDS detector to a recently developed annular EDS detector, when analyzing electron transparent and beam sensitive NaCl particles on a TEM grid. The optimal settings for single particle analysis are identified in order to minimize beam damage and optimize sample throughput, via choice of acceleration voltage, EDS acquisition time, and quantification model. Here a linear combination of two models is used to bridge results for particle sizes, which are neither bulk nor sufficiently thin to assume electron transparent. Additionally, we show that the increased count rate obtainable with the annular detector enables mapping as a viable analysis strategy compared to feature detection methods, which only scan segmented regions. Finally, we discuss advantages and disadvantages of the two analysis strategies.

## Introduction

Scanning electron microscopy (SEM) is capable of imaging samples with nanometer resolution, providing size and morphology information. When coupled with energy dispersive X-ray spectroscopy (EDS), the method can also identify and quantify elements heavier than lithium (Hovington *et al.* 2016), by detection of electron-excited characteristic X-rays. This makes SEM/EDS a powerful characterization tool applied in a broad range of fields including environmental (Kandler *et al.* 2009; Kling *et al.* 2016; Laskin *et al.* 2006; Laskin & Cowin 2001), material (Arepalli *et al.* 2004; Lee *et al.* 2004; Sathirachinda *et al.* 2010), and health sciences (Koh *et al.* 2008; Lee *et al.* 2015; Stebounova *et al.* 2011). The method is, however, subject to many sample specific uncertainties including morphological effects, sample-matrix interactions, and radiolytic beam sensitivity. Users therefore have to choose the optimal microscope settings prior to analysis, as well as the best-suited model and algorithms for quantification during data treatment. Here microscope settings include aperture size, spot size, acceleration voltage, and EDS acquisition time. Choices during data treatment mainly refer to the quantification model, though the quality of background X-ray subtraction, deconvolution, and peak fitting procedures also have a significant influence on the results (Newbury & Ritchie 2013, 2014). These choices strongly affect the success of the analysis and the

quality of results. Preferably, the choices should be evaluated on a case-by-case basis depending on sample and available equipment.

This study provides guidance on identifying settings and parameters of highest relevance for single particle analysis of thin electron transparent and beam sensitive samples. Recommendations include choice of acceleration voltage, EDS acquisition time, as well as quantification model, where a comparison is made between Cliff-Lorimer (for electron transparent samples) and P/B-ZAF (for bulk samples). Here, a simple expression is used to bridge quantification results from particles in the size range transitioning from electron transparent to bulk sizes. The analyzed samples consist of NaCl particles in the size range 50-500 nm collected onto TEM grids. NaCl was chosen, firstly as it is present in many types of samples such as biological and environmental samples, and secondly because it is a beam sensitive compound, like most alkali halides. This causes difficulties for standard EDS detectors, due to degassing of halides from the NaCl surface upon extended beam exposure(Allen *et al.* 1998; Cazaux 1995; Egerton *et al.* 2004).

Additionally, a comparison is made between a traditional side mounted EDS 30 mm<sup>2</sup> Silicon Drift Detector (SDD) and a newly developed annular EDS 4 × 15 mm<sup>2</sup> SDD, situated between the pole piece and the sample. The new detector configuration achieves a much higher solid angle and significantly higher X-ray count rates than previous designs(Brodusch *et al.* 2018). This reduces the needed acquisition time without sacrificing counts. The increased count rate also makes it possible to map the entire imaged area within a reasonable timeframe, as opposed to limiting the EDS analysis to a selected subset of pixels – often referred to as feature analysis or particle detection(Teng *et al.* 2018). The study concludes with a comparison of mapping and feature analysis, highlighting available options and discussing the advantages and disadvantages of the two strategies when analyzing electron transparent samples.

## **Materials and Methods**

### **Aerosol Generation and Collection**

The sampled aerosol was generated with a constant output atomizer model 3076 (TSI, USA), which was operated at a backpressure of 2 bar. The atomizer generated aerosols from a solution of 1 g NaCl (purity ≥99.0%, Sigma-Aldrich, USA) in 500 ml nanopure water. From the atomizer, the aerosol was passed through two diffusion driers model 3062-NC (TSI, USA) installed with freshly dried silica gel, decreasing the relative humidity from 100 to less than 10%. The dried aerosol was sent into a small Plexiglas chamber of approximately 0.5 m<sup>3</sup>. A scanning mobility particle sizer (SMPS) was used to monitor the total number concentration in the chamber, which consisted of a differential mobility analyzer model 3082 (TSI,USA) and a condensation particle counter model 3776 (TSI, USA). The SMPS was operated in low flow mode (0.3 l/min) with a sheath to aerosol flow ratio of 10. The aerosol was sampled from the chamber with a 3-stage cascade impactor, using a diaphragm gas pump model NMP 830 (KNF Neuberger, Germany). The aerosol was sampled at a flow rate of 0.76 L min<sup>-1</sup>, giving impactor D<sub>50</sub> values of 1.36, 0.59, and 0.073 μm for the three stages respectively. Each stage was fitted with commercially available 400 mesh nickel TEM grids coated with a 25-50/1

nm Formvar/Carbon film (Electron Microscopy Sciences (EMS), USA). This allowed the atomized NaCl particles to be collected directly onto TEM grids and analyzed by SEM without additional preparatory steps. Appropriate particle coverage was achieved by sampling for 5 seconds at a total number concentration of approximately  $3.5 \times 10^5 \text{ cm}^{-3}$ , as measured by the SMPS. This fits well with the sampling recommendation of Brostrøm *et al.* (Brostrøm *et al.* 2019). Particles were only observed on the lowest impactor stage, consistent with the expected 100-200 nm sizes, as the lowest stage collects particles with diameters from 73 to 590 nm (Brostrøm *et al.* 2019).

### **Electron Microscope**

The sampled grids were analyzed in high vacuum (HV) mode with an Everhart-Thornley secondary electron detector in a Nova NanoSEM 600 (Thermo Fisher Scientific (former FEI), The Netherlands). The microscope is equipped with both an XFlash 6|30 and an XFlash FlatQuad (Bruker Nano, Germany) EDS detector. The XFlash 6|30 (from here on referred to as XFlash) is a 30 mm<sup>2</sup> SDD delivering an energy resolution of 123 eV at Mn K $\alpha$ . The detector is placed 44 mm from the sample surface, with a take-off angle of 35°, and a corresponding solid angle of 0.0119sr. The XFlash FlatQuad (from here on referred to as FlatQuad) is a 60 mm<sup>2</sup> retractable annular detector situated between the pole piece and the sample, with a take-off angle of 60°. The FlatQuad has an optimal sample to detector distance of 3 mm (see SI), which was used in this study, corresponding to a solid angle of 0.95sr. The FlatQuad is designed with a center hole for the incident electron beam to pass through and with four individual 15 mm<sup>2</sup> SDD quadrants mounted radially around it (see SI), reaching an energy resolution of 126 eV at Mn K $\alpha$ . The four quadrants make the detector insensitive to potential sample shielding effects upon positioning, and achieve a much higher solid angle than the XFlash. A schematic of the two detector configurations is shown in the SI.

For all SEM/EDS analyses, the ESPRIT 2 software (Bruker Nano, Germany) was used. The necessary detector dead-times were estimated automatically by ESPRIT for each particle, based on the measured counts per second (cps). For the XFlash, dead-times were almost exclusively 0% due to the relatively low cps. Measurements with the FlatQuad had a mean dead-time of  $3.7 \pm 2.5\%$ , though the largest particles had dead-times as high as 25%. Since the FlatQuad is situated directly above the sample, it is also exposed to high-energy electrons emitted from the sample. The FlatQuad is therefore equipped with a Mylar shield to absorb the incoming electrons. The thickness of the shield is increased with acceleration voltage, since more energetic electrons are emitted from the sample. The available thicknesses are 1, 1+2, and 1+6  $\mu\text{m}$  Mylar for acceleration voltages below 6, 12, and 20 keV respectively. Along with the high-energy electrons, a fraction of the low energy X-rays will also be absorbed by the shield, depending on its thickness. As a result, the detection of X-rays is limited by acceleration voltage in the high-energy region, and by absorption from the Mylar shield in the low energy region. These effects are accounted for automatically in the ESPRIT software fitting procedures, but with the thickest shield it is not possible to quantify elements lighter than F. The FlatQuad detector was not inserted when performing EDS with the standard XFlash detector as it would block the X-rays leaving the sample.

The microscope was operated at acceleration voltages of 5, 10, or 20 keV, with an aperture size of 50  $\mu\text{m}$ , and a spot size setting of 3.5, resulting in probe currents of 0.11, 0.16, and 0.19 nA for the three voltage settings, respectively. All SEM/EDS analyses were performed at 10k-12k on-screen magnification with pixel resolutions of approximately 7.1 nm/pixel.

To distinguish NaCl particles from the substrate, images were segmented using a fixed global threshold. The segmentation and EDS analysis was performed in two different ways for comparison:

- a) Feature analysis: Image segmentation is made prior to EDS analysis, in order to distinguish particles from the substrate and limit analysis to pixels recognized as particles. The beam is set to scan the entire area of each particle and acquisition times are set as livetimes, referring to the beam exposure time per particle regardless of its size.
- b) Mapping: An EDS map of the entire image is acquired and image segmentation is performed as a post processing step. For maps, the acquisition time is set as a dwelltime, referring to the beam exposure per pixel, as particles are not yet distinguished from the substrate.

In both cases, spectra of all individual pixels within the contour of a single recognized particle were summed and analyzed as one. To remove the bremsstrahlung X-ray contribution from spectra, a background was fitted and subtracted before further analysis. The background fit was performed using the SEM fitting option available with the ESPRIT software, where areas suitable for fitting (areas without peaks) were identified automatically. The fitting curve follows the shape of a bremsstrahlung X-ray background, taking into account absorption of low energy X-rays in the detector window and electron shield. Generally, the automated post processing algorithms functioned well, but in isolated cases, the procedures fitted the background to areas with peaks, or completely missed relevant peaks. Therefore, all individual particle spectra were manually inspected and critically evaluated on a case-by-case basis before trusting the results. Data handling, processing, and visualization of the EDS results were performed with Python 3.6.

### **Quantification Methods**

Quantification models are needed to convert measured X-ray counts to concentrations in the form of mass or atomic percentages. There are several different quantification models available with commercial EDS software, though it is not always considered how big an influence the models have on the determined concentrations or which model to use for which samples.

The most common quantification method for EDS analysis is the P/B-ZAF method, which allows for a standardless, semi quantitative analysis, while taking into account matrix interactions, such as fluorescence and absorption(Wendt 1978; Wendt & Schmidt 1978). It is used for bulk, polished, and homogeneous samples. However, for thin specimens the X-ray-sample interaction is very limited and most matrix effects should be ignored as it can lead to unnecessary corrections. In this study we compare results from P/B-ZAF to the Cliff-Lorimer model(Cliff & Lorimer 1975), which is better suited for thin samples. Both methods are available in the ESPRIT software.

P/B-ZAF is a true standardless method as opposed to the standard based ZAF(Armstrong & Buseck 1975), where a reference sample with known composition is needed for quantification. Instead, P/B-ZAF uses the characteristics of the bremsstrahlung X-rays in the sample spectrum as a reference – hence using the spectrum background (B) as a reference for a given peak (P). The ESPRIT software determines the weight fraction of elements by iterative comparison between a standard database and the solutions to a set of nonlinear equations, taking the form of Eq. (1).

$$(1) \left(\frac{P}{B}\right)_i = \frac{I_{i,char}}{I_{i,br}} = c_i * \omega_i * q_i * \frac{(Z*A*F)_{i,char}}{(Z*A)_{i,br}}$$

Where  $I_{i,char}$  and  $I_{i,br}$  are the number of characteristic and bremsstrahlung X-rays of an element  $i$  in a sample, while  $c_i$  is the mass fraction,  $\omega_i$  is the fluorescence yield, and  $q_i$  is the relative emission rate of the given energy transition within element  $i$ . The Z, A, and F factors correct for sample matrix influences, where Z corrects for stopping power and backscattering effects which are atomic number dependent(Duncumb & Reed 1968), while the A and F factors correct for self-absorbing and fluorescence effects(PHILIBERT 1963; Reed 1965).

For thin specimens, the produced X-rays have a low probability of interacting with the sample, making it possible to ignore absorption and fluorescence effects. The Cliff-Lorimer method relates the weight fractions ( $c$ ) of elements A and B to the measured number of characteristic X-rays ( $I$ ) by a Cliff-Lorimer factor  $K_{AB}$ , using Eq. (2).

$$(2) \frac{c_A}{c_B} = K_{AB} \frac{I_A}{I_B}$$

By convention Cliff-Lorimer factors are given relative to silica, so the factor for any two elements can be determined from the ratio of their silica factors using Eq. (3). For samples containing more than two elements Eq. (3) and (4) are needed, which can be combined with Eq. (2) for the multi element expression in Eq. (5):

$$(3) k_{AB} = \frac{k_{AC}}{k_{BC}}$$

$$(4) \sum_{i=A,B,C..} c_i = 1$$

$$(5) c_A = \frac{K_{ASi} * I_A}{\sum_{i=A,B,C..} K_{iSi} * I_i}$$

The Cliff-Lorimer factor  $K_{iSi}$  depends on both instrument and element specific factors, but it is independent of sample composition. The factors can therefore be determined for all instrument settings, either experimentally or through theoretical calculation. The experimental factors are more precise, reaching relative errors as low as 1%, while the theoretical factors can have systematic relative errors as high as 15-20%(Watanabe & Williams 2006). However, multiple standard thin-film samples with known composition are required to determine the experimental factors. The typical choice in most studies is the standardless P/B-ZAF and theoretical Cliff-Lorimer factors, and these are used in this work.

The two models can be used to quantify either bulk or electron transparent samples, but both fail in the particle size range transitioning from transparent to bulk sizes, as shown by Laskin *et al.* (Laskin *et al.* 2006). To overcome this issue, Kandler *et al.* (Kandler *et al.* 2018) recently proposed a simple method, where results from the two models are interpolated as a function of particle size. In the method, particles smaller than a threshold value (1.5  $\mu\text{m}$ ) are quantified by Cliff-Lorimer, while particles larger than another threshold value (30  $\mu\text{m}$ ) are quantified by P/B-ZAF. In the size range between the two values, particles are quantified with both models and the results are weighted based on particle size and summed. The method was developed based on samples of polished NaCl crystals analyzed at 20 keV. The proposed method is therefore only valid for NaCl at 20 keV, since lowering the acceleration voltage or analyzing a sample with a higher density than NaCl, will shrink the interaction volume. As a result, smaller particles will act as bulk samples, making P/B-ZAF valid at sizes below 1.5  $\mu\text{m}$ . Here it should be noted that a smaller interaction volume means that X-rays are produced closer to the particle surface, thereby reducing their sample interaction. Results from P/B-ZAF and Cliff-Lorimer quantification will therefore be more similar at small interaction volumes. Also, the difference between P/B-ZAF and Cliff-Lorimer results is lower for high energy X-rays, which are not absorbed as readily as X-rays with energies below approximately 2 keV (Fletcher *et al.* 2011).

We propose an alternative interpolation method, where the depth of the interaction volume is considered when determining the P/B-ZAF and Cliff-Lorimer weights. We argue that particles larger than or equal to the depth of the interaction volume should be quantified as bulk samples, using P/B-ZAF. In addition, we argue that particles with a size of half the depth of the interaction volume should have equal weights for the two models. This gives a simple linear expression for the weights:

$$(6) X = \begin{cases} D_p < D_i, & \frac{D_p}{D_i} * X_{ZAF} + \left(1 - \frac{D_p}{D_i}\right) * X_{CL} \\ D_p \geq D_i, & X_{ZAF} \end{cases}$$

Where  $X$  is the corrected concentration of a given element in the interaction volume,  $D_p$  is the estimated particle thickness e.g. equivalent diameter,  $D_i$  is the depth of the interaction volume, while  $X_{ZAF}$  and  $X_{CL}$  are the element concentrations quantified using P/B-ZAF and Cliff-Lorimer respectively. As discussed, the depth of the interaction volume is influenced both by sample characteristics and the acceleration voltage, but it can be estimated using the simple approach of Potts (Potts 1987):

$$(7) D_i = \frac{0.1 * E_0^{1.5}}{\rho}$$

Here  $E_0$  is the acceleration voltage of the incident beam and  $\rho$  is the sample density (2.16  $\text{g}/\text{cm}^3$  for NaCl). Ideally, the weights should be determined from the interaction and particle volumes, accounting for particle geometry and adjusting according to the X-ray path within each individual particle relative to bulk and transparent samples. However, such assessments require complex calculations or simulations, as the size and shape of both particle and interaction volume are difficult to measure. A method using this approach was proposed by Ro *et al.* (Ro *et al.* 2003), though it

requires extensive Monte Carlo simulations and is thus not yet applicable for large datasets. The more simplistic correction based on particle size and interaction depth ratio is therefore proposed as a first order correction, though it may introduce some bias. The bias may be significant for high aspect ratio particles, where the particle and interaction volume widths are also relevant for assessing the X-ray path within particles. Finally, some bias may result from scanning the beam across particles, as opposed to stationary measurements at the particle center. This will generally reduce the mean X-ray path within particles, as X-rays can be generated near the particle surface or edge during a scan.

## Results and Discussion

A series of images was acquired of the NaCl samples at 5, 10, and 20 keV. The ESPRIT software *feature analysis* was used for automated image acquisition, image segmentation, and subsequent EDS analysis of the individual particles. At each voltage, three different image/EDS procedures were performed with particle livetimes of 1, 5, and 15 seconds respectively. For the 15 seconds livetime setting, the total number of particles for EDS analysis was limited to 100, in order to reduce the overall acquisition time. These analyses were performed both with the XFlash and FlatQuad detectors, but in different areas of each sample to avoid accumulated beam damage. A table of all 18 setting combinations is shown in the SI, along with nine SE images of the areas used for EDS analysis with the XFlash detector. Results from a feature analysis performed at 20 keV with the FlatQuad using 15s livetime is shown in Figure 1.

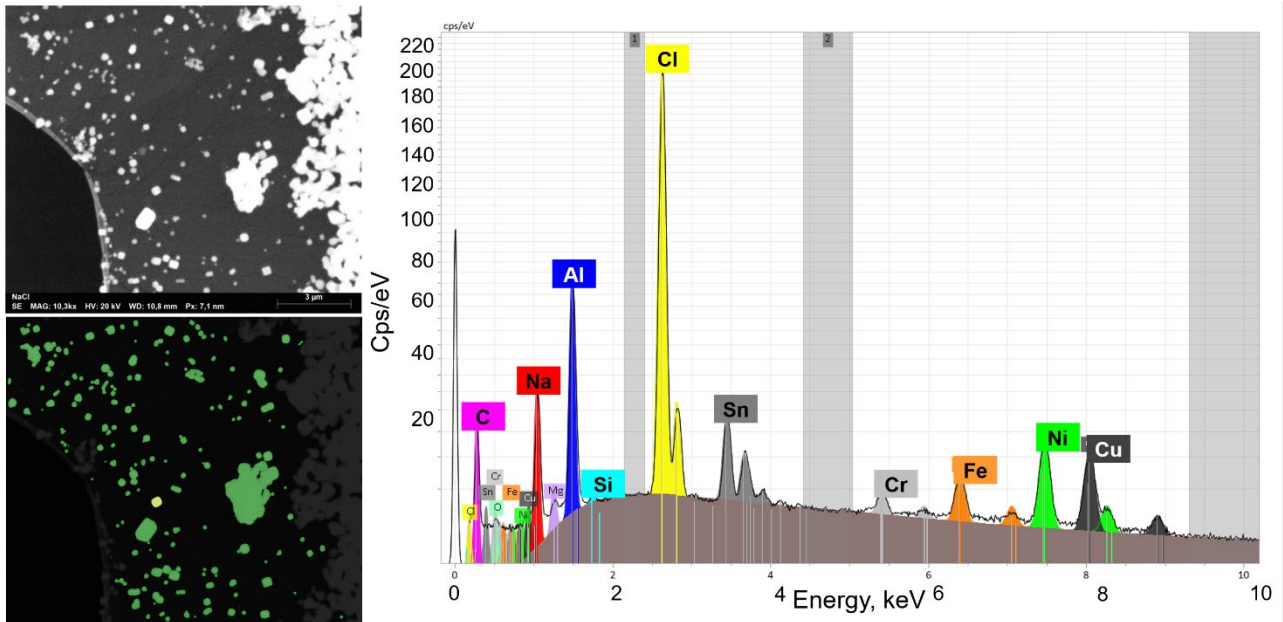


**Figure 1. Top left: SE image of the NaCl sample at 20 keV. Top Right: Segmented SE image, where all pixels categorized as particles are marked in green. Bottom: The EDS spectrum of the particle marked in yellow on the segmented SE image. The original spectrum is in black, while the fitted background is in dark grey at the bottom. The areas used for fitting the bremsstrahlung background are marked as light gray columns. Fitted element peaks are presented in various**

colors with the name of the element written above the primary peak. Element specific emission lines are also presented as thin vertical lines in the bottom of the spectrum using the element respective colors, with the height of the line indicating its relative intensity. X-rays are binned into 5eV energy bins and the y-axis is square root scaled for easier visualization.

From the spectrum, it is seen that many elements apart from pure NaCl are detected, including Al, Si, Sn, Cr, Fe, and Cu. These elements can be attributed to the setup as transmitted or stray electrons hit the sample holder, detector housing, or microscope chamber. A substantial carbon peak is also visible, which originates from the Carbon/Formvar substrate and to a lower extent from potential volatile organic compound contamination. The spectrum was quantified using Cliff-Lorimer, which gave the atomic percentages presented in Table 1. Here oxygen was included in the fitting procedures, but was deconvoluted prior to determining atomic percentages, as it has a very low X-ray yield, making it difficult to quantify. Oxygen concentrations are therefore often determined based on stoichiometry rather than X-ray count (Newbury & Ritchie 2014).

**Table 1. Table of element quantification results from the EDS spectrum in Figure 1 along with errors estimated by the ESPRIT software. Oxygen was included in the fitting procedures during quantification, but was deconvoluted before determining mass and atomic concentrations as the oxygen signal is highly uncertain in EDS.**

Element	At. No.	X-ray Count	Atomic%	Abs. error, % (1 sigma)	Rel. Error, % (1 sigma)
C	6	14807	68,22	2,16	3,17
Na	11	27449	10,73	0,35	3,26
Cl	17	312575	7,72	0,25	3,19
Ni	28	3096	5,37	0,56	10,34
Al	13	77223	5,31	0,18	3,36
Cu	29	27879	0,81	0,03	4,03
Mg	12	4953	0,66	0,04	6,40
Sn	50	41905	0,61	0,70	10,70
Fe	26	17299	0,35	0,02	5,62
Cr	24	8191	0,14	0,01	10,09
Si	14	1572	0,07	0,02	26,29
O	8	15	-	-	-

As seen from Table 1, the dominating element is C, while the two second most abundant elements are Na and Cl, which fits well with the expected pure NaCl particle on a carbon substrate. Substantial concentrations are also detected of Ni, originating from the Ni TEM grid, and Al, originating from the microscope and sample holder, which is made of Aluminum. The aluminum signal could thus be reduced by installing e.g. a carbon-based object (shield) underneath the sample to absorb transmitted electrons, or by exchanging the sample holder material. The remaining elements were identified as trace elements, making up less than 1 At% each, and environmental particles with these

components would therefore still be distinguishable. It should however be noted that the absorption of low energy X-rays by the thick Mylar shield necessary at 20 keV, makes the quantification of light elements such as C highly uncertain. This uncertainty is not captured in the error estimates of the ESPRIT software in Table 1.

### Detector Comparison

A common challenge in EDS analysis is the number of counts needed to obtain a sufficient precision. For example, 10k, 2.5k and 0.4k counts in a peak are needed to reduce the relative uncertainty of the element fraction to 1, 2, or 5%, when based on counting statistics alone. For relatively low solid angle detectors such as the XFlash, it is challenging to reach peak counts higher than 1000 within the short acquisition times necessary for beam sensitive compounds. However, when positioning detectors between the pole piece and the sample as for the FlatQuad, a much greater solid angle is achieved, increasing the X-ray count rate substantially. To demonstrate the outcome of the two detector designs, the EDS spectra of NaCl particles with an equivalent circular diameter ( $D_{eq}$ ) of approximately 100 and 500 nm at 5, 10, and 20 keV, using either 1 or 15s livetime for both the XFlash and FlatQuad detectors are presented in Figure 2. The spectra are presented without background subtraction, which is why the 5 keV spectra drop to zero counts at 5 keV, as the incident electrons cannot generate X-rays with energies higher than the beam. An overview table showing voltages, livetimes, particle sizes, and the integrated X-ray count from 100 eV to the incident beam for each spectrum in Figure 2 can be found in the SI.

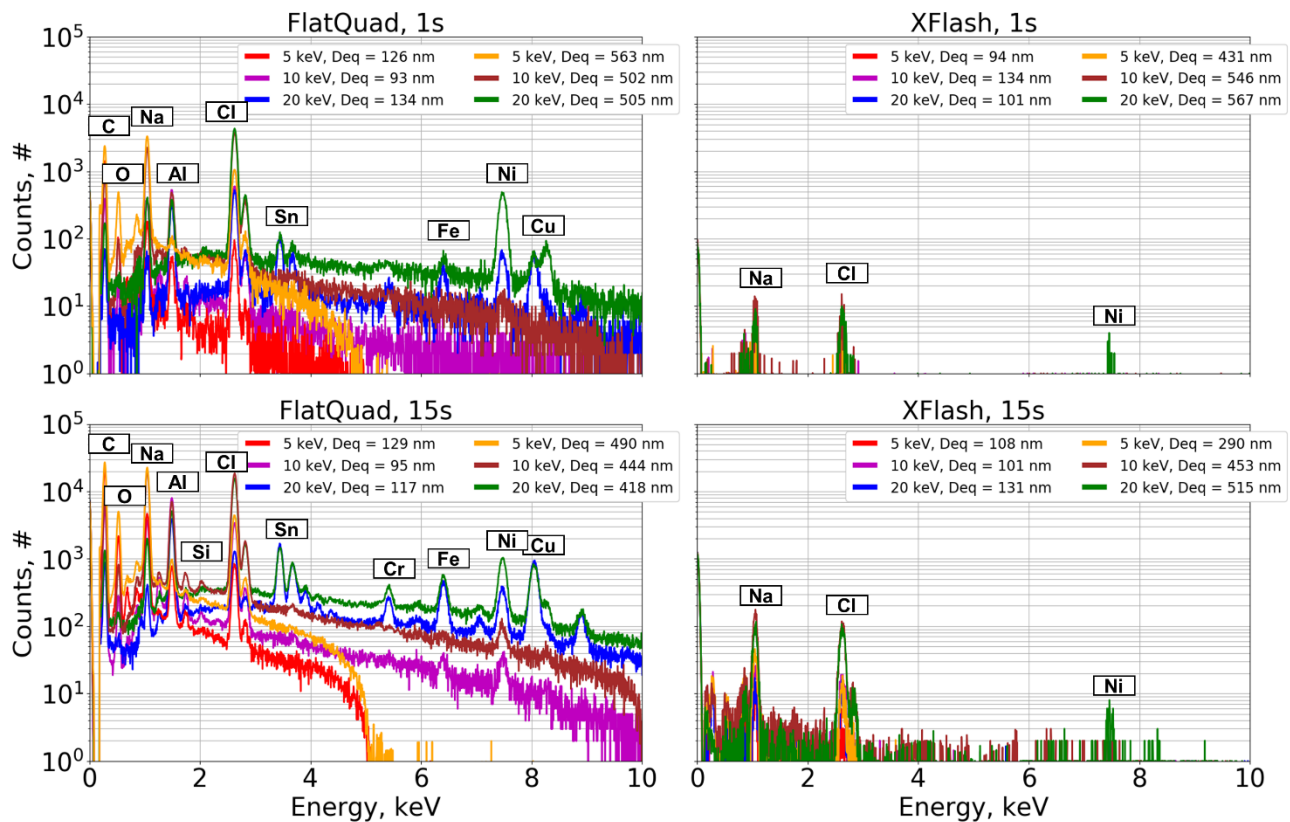


**Figure 2. EDS spectra of NaCl particles with Deq of approximately 100 and 500 nm acquired at 5, 10, or 20 keV, using either 1 (Top row) or 15s (Bottom row) livetime for the FlatQuad (Left column) and the XFlash (Right column). The Deq of the corresponding NaCl particles are shown in the legend. Y-axis is in log scale, showing the total number of X-ray counts during the entire acquisition period, for each 5eV energy bin.**

As seen from Figure 2, the number of counts in the FlatQuad spectra are several orders of magnitude higher than for the XFlash when operating at similar conditions. As a result, the FlatQuad spectra display clearly distinguishable element peaks containing thousands of counts, while the XFlash can barely detect the major components Na and Cl at 1s livetime. Furthermore, the number of bremsstrahlung X-rays are limited for the XFlash when using short acquisition times, which complicates background fitting and subtraction procedures.

To investigate which settings allow for low relative errors compared to the acquisition time, the number of X-rays detected in the Na peak of each particle EDS spectrum, are plotted against the particle area in pixels in Figure 3. The plot includes all combinations of acceleration voltage, livetime, and detector type. All elements listed in Table 1 were included in the identification list, and the Na X-ray counts were determined after background subtraction. A boxplot of the Na X-ray count for the two detectors, which have been normalized by particle area and livetime, can be found in the SI.

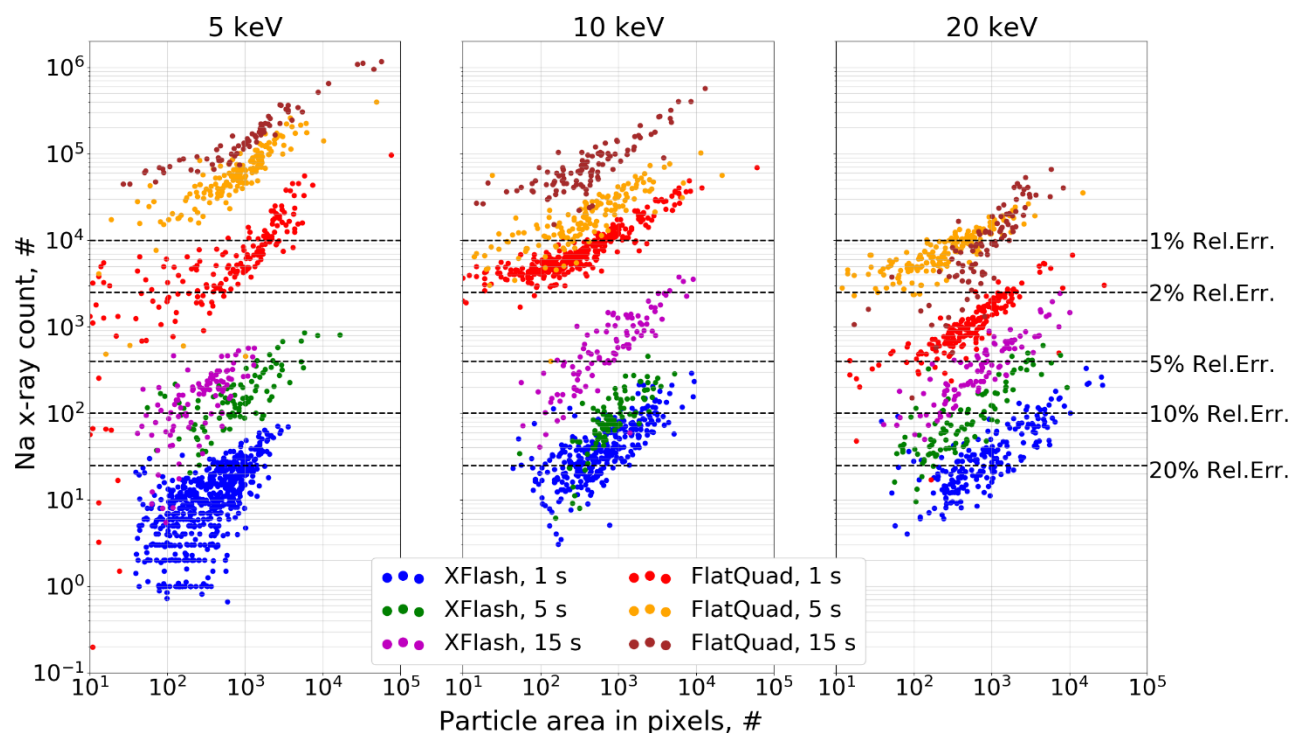


**Figure 3. Total X-ray counts in the Na peak for each individual particle spectrum after background subtraction, for all combinations of acceleration voltage, livetime, and detector, plotted against particle size in pixels. The dashed black lines mark 1, 2, 5, 10, and 20% relative error based on**

**counting statistics as  $\sqrt{N}$ , where N refers to the number of detected Na X-rays. Pixel size was approximately 7.1 nm for all images.**

From Figure 3 it is seen that the number of X-ray counts in the Na peak is highly dependent on particle size, as more electrons will pass through smaller particles with zero loss, resulting in lower X-ray yields. Here, it should also be noted that though EDS livetime is constant, the dwelltime is not. This means that small particles consisting only of a few pixels are scanned more intensively during the same livetime, making them particularly susceptible to beam damage.

It is furthermore seen from Figure 3 that an increase in acceleration voltage does not necessarily result in higher X-ray counts for electron transparent samples, as would be expected for most bulk samples. A part of the reduced counts may result from a higher absorption of the low energy Na  $K\alpha$  X-rays (1.040 keV), when traversing the thicker detector shield at 20 keV relative to 5 keV. This reduction is however accounted for in the quantification algorithm of the Esprit software. The lower counts may also result from the increased penetration depth of the more energetic electrons, which, for thin samples, means that more electrons are transmitted without detectable interaction (Friel & Lyman 2006). The change in interaction volume was exemplified by performing Monte Carlo simulations of electron interaction with flat bulk NaCl samples, using Casino v3.3 (Demers *et al.* 2011). Here a maximum penetration depth of approximately 0.4, 1.3 and 4  $\mu\text{m}$  respectively was found when simulating 10000 electron trajectories at acceleration voltages of 5, 10, and 20 keV. Images from the simulation are shown in the SI. As the average equivalent diameter of the NaCl particles analyzed in this study is  $215 \pm 205$  nm, the 10 and 20 keV settings will have a significantly higher fraction of zero loss electrons. This effect is however mitigated slightly by the corresponding increase in probe current, which rises from 0.11 to 0.16 and 0.18 nA for 5, 10, and 20 keV respectively. The net effect is an inverse relation between X-ray count and voltage, with the highest counts obtained at 5 keV, though the effect is not visible for the low counts of the XFlash detector.

Overall, it is clear that the livetime needed to ensure relative errors below e.g. 2%, can be decreased by orders of magnitude when using the FlatQuad detector compared to the XFlash. Even the 15s livetime for the XFlash is approximately an order of magnitude lower in counts, compared to the FlatQuad at 1s livetime. This reduces the overall EDS analysis time from hours to minutes and opens for new possibilities such as mapping of the entire image, rather than limiting EDS to pixels recognized as particles.

For comparison of the quantified results, all spectra were analyzed using the Cliff-Lorimer model, and the resulting Na and Cl at% were plotted against each other for all settings in Figure 4. Here it should be noted that the higher Na and Cl concentrations measured with the XFlash compared to the FlatQuad are partly due to the detector and sample holder configuration. The XFlash is located slightly behind the bulk sample holder and is therefore shielded from X-ray emissions below the sample. In contrast, the FlatQuad is mounted directly above the sample, thereby detecting most X-

rays emitted from below, resulting e.g. in higher Al counts and a corresponding reduction in the relative Na and Cl at%.

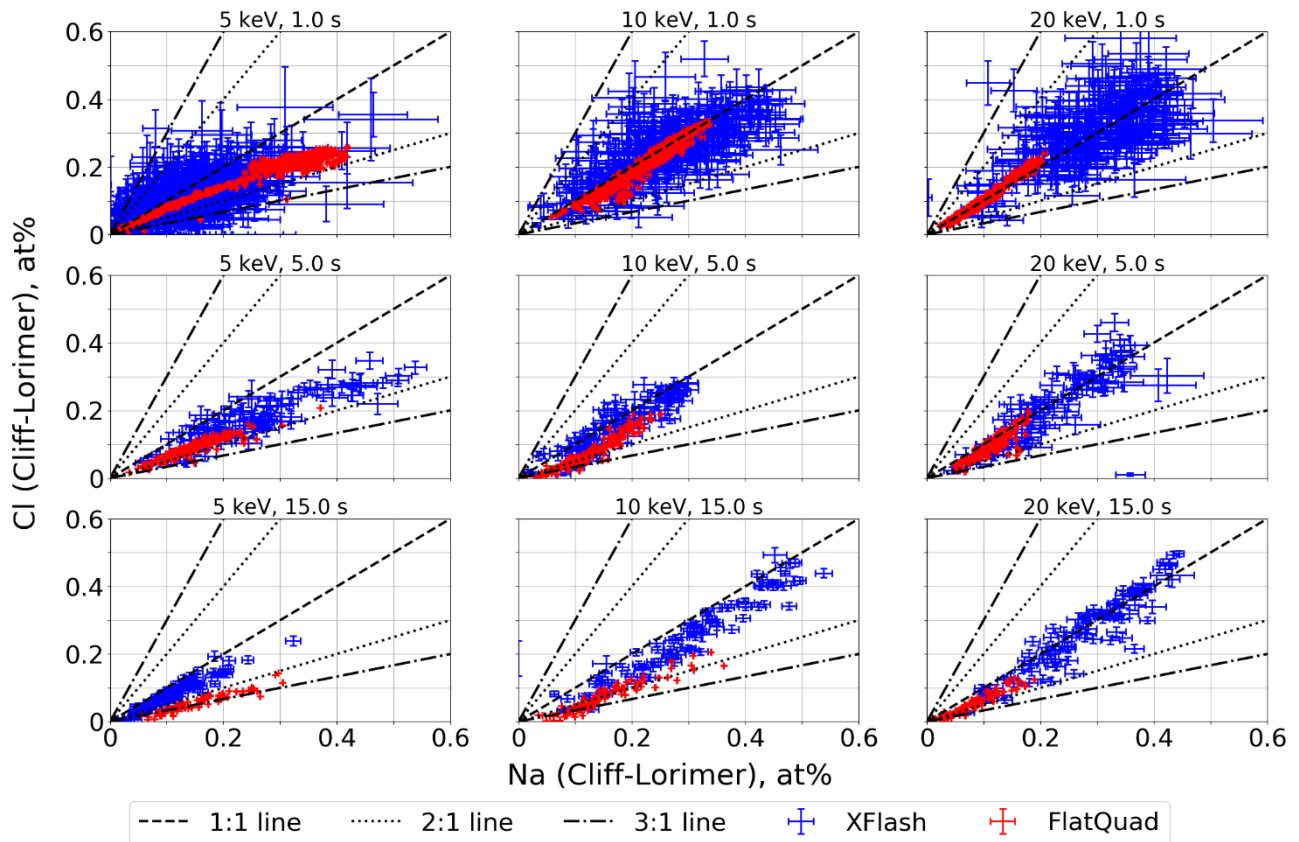


**Figure 4.** Plot of Na at% against Cl at% for the XFlash (blue) and FlatQuad (red) quantified with Cliff-Lorimer. Error bars were determined based on counting statistics as  $\sqrt{N}$  from the number of X-ray counts in the Na or Cl spectrum peaks. Lines corresponding to ratios of 1:1, 2:1, and 3:1 have also been plotted as reference.

When comparing results from the two detectors it is clearly seen that the low counts of the XFlash detector give major uncertainties at 1s livetime, whereas the FlatQuad detector provides consistent results, following clear trends. As the livetime is increased, the uncertainties of the individual XFlash data points are reduced, but they still display a larger spread than for the FlatQuad. The higher consistency of the FlatQuad results reveals systematic deviations from the 1:1 line, which are partly obscured in the XFlash results. These deviations are related to beam damage and quantification model, which will be discussed in the following sections.

### Beam Sensitivity

The influence of beam damage is seen in Figure 4, when comparing plots in the same column. Here the same microscope settings are used, but the beam exposure is varied. Upon longer exposure the particle's composition shift from values close to the 1:1 line at 1s livetime, towards the 2:1 and 3:1 lines at 5 and 15s livetime. All observed shifts correspond to an enrichment in Na relative to Cl,

which is consistent with the loss of halides upon beam radiation, as reported in the literature(Allen *et al.* 1998; Cazaux 1995; Egerton *et al.* 2004).

It is furthermore seen that the beam damage is most severe at 5 keV, where the Na/Cl ratio shifts from the 1:1 line at 1s livetime to the 1:3 line at 15s. In comparison, the ratio only shifts to the 1:2 line at 20 keV. The smaller shift is due to a higher number of transmitted electrons at 20 keV compared to 5 keV. At 5 keV, the majority of the interaction volume is within e.g. a 300 nm particle, which results in a higher degree of beam damage. However, a shift to the 1:2 line at 20 keV and 15s livetime still indicates a significant beam influence upon extended livetime. This can also be observed directly when comparing images before and after EDS analysis, which can be seen in Figure 5, where the NaCl sample analyzed at 20 keV with 15s livetime is shown.

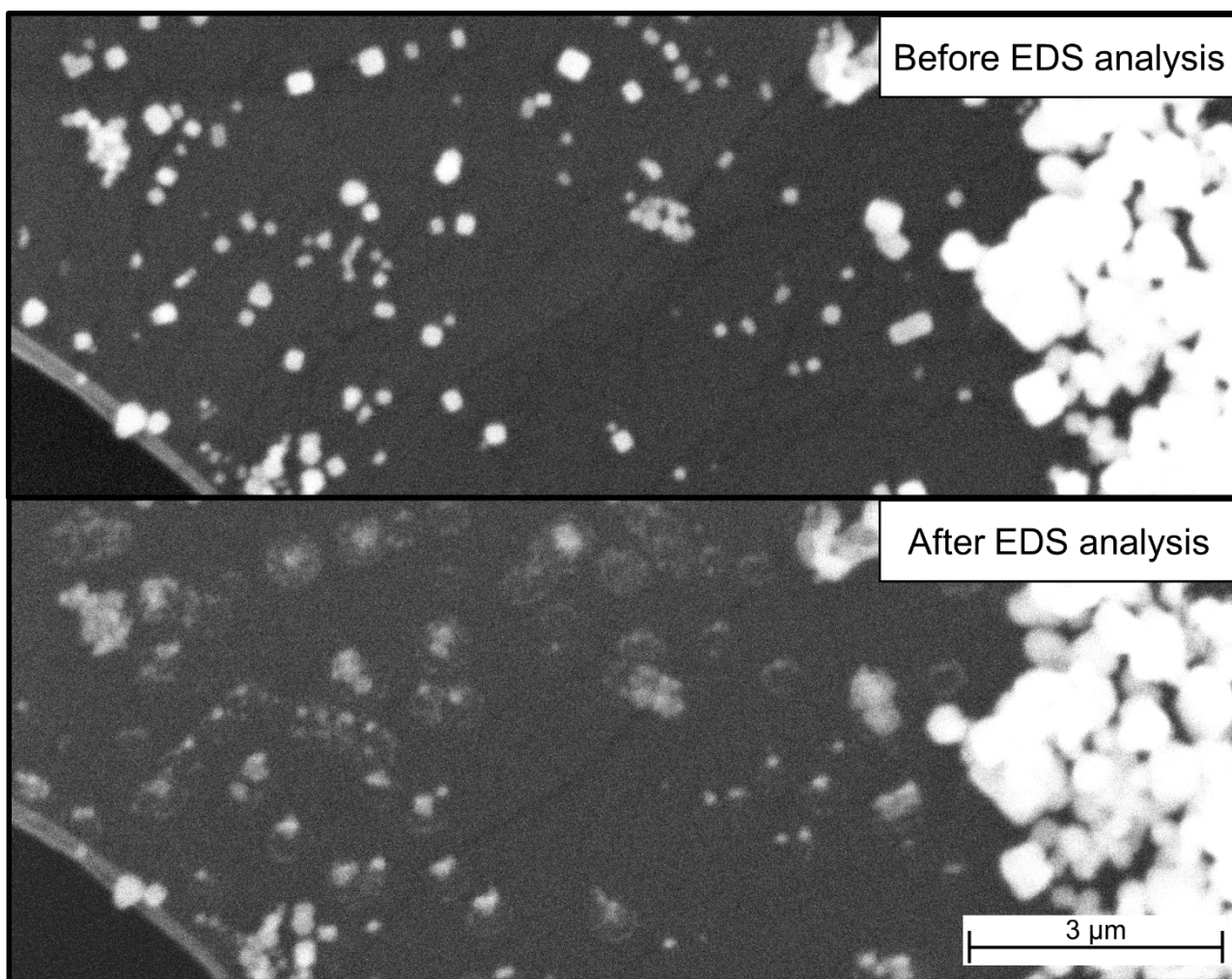


**Figure 5. SE images of NaCl particles before (top) and after (bottom) EDS analysis performed at 20 keV with a particle livetime of 15s. Pixel resolution was 7.1 nm.**

Figure 5 clearly shows the severity of beam damage for NaCl, with most of the particles transformed to craters after the EDS analysis. Even particles of a few hundred nm have almost completely disappeared during the 15s livetime, while many of the smaller particles are no longer visible. It is

therefore obvious that beam exposure can alter the shape, size, and elemental composition of a beam sensitive sample.

To further investigate the beam effects, a series of 15 consecutive EDS measurements with a 1s livetime were conducted at 10 keV in the same area of the sample. This made it possible to quantify the Na and Cl concentration of selected particles with a range of sizes and plot them as a function of beam exposure, as seen in Figure 6.

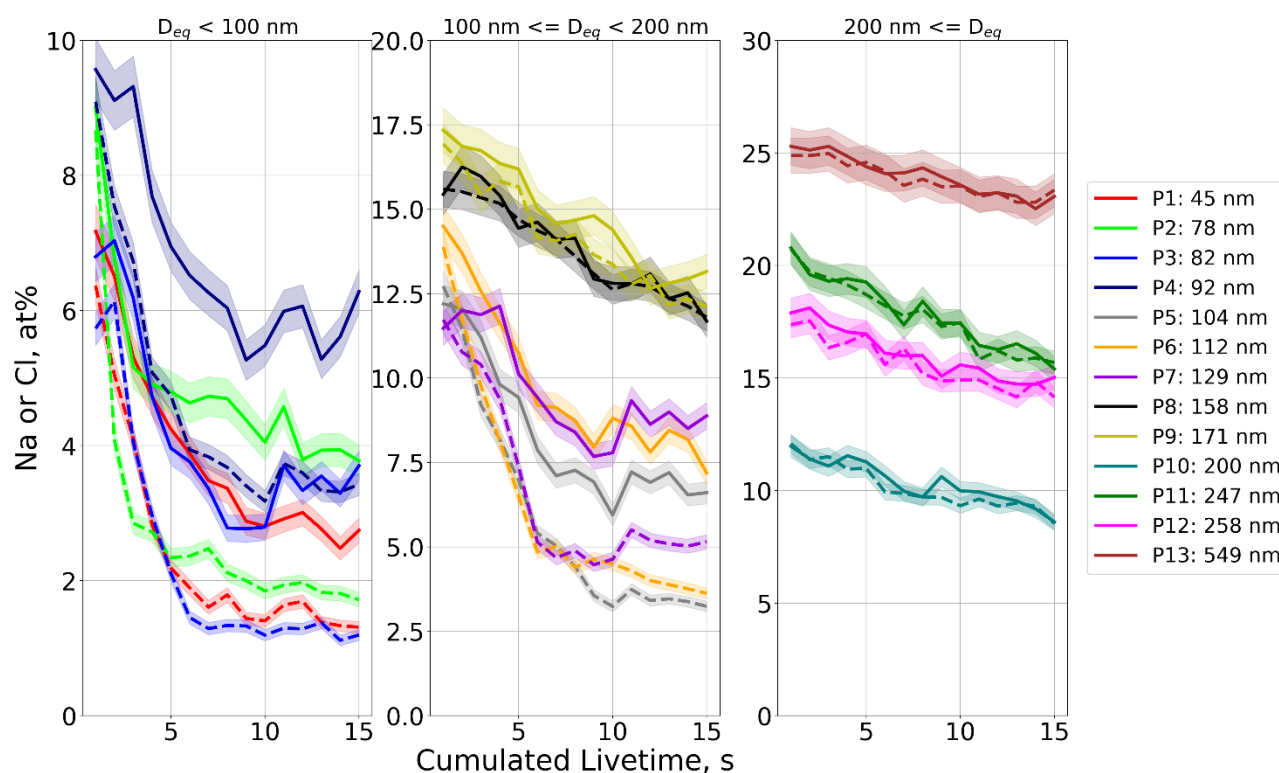


**Figure 6.** The Na (solid lines) and Cl (dashed lines) atomic percentages from 15 consecutive EDS measurements at 10 keV for a selection of 13 NaCl particles with sizes ranging from approximately 50 to 550 nm. The Cliff-Lorimer model was used for quantification and the shaded areas represent uncertainties determined from counting statistics ( $\sqrt{N}$ ). Particle sizes are reported as equivalent circular diameters. It should be noted that the y-axis is scaled differently in the three plots.

From the three plots in Figure 6, it is seen that the Na and Cl concentrations are similar at 1s livetime for all particles, consistent with the expected 1:1 ratio. However, as the beam exposure continues, both the Na and Cl content decrease, regardless of particle size. The relative decrease is most severe for particles smaller than 150 nm. These particles experience a reduction to approximately half their original concentration during the 15s exposure, corresponding to a drop of 4-6 at% in Na and Cl. Larger particles show a similar decrease, but as their initial concentration is higher, the relative drop is smaller. It is furthermore seen, that Cl is depleted faster than Na in particles below 150 nm, while it follows the Na depletion in larger particles. The different depletion rates could be related to the higher surface to volume ratio in small particles, causing a faster Cl evaporation. However, when comparing the results of Figure 4 and Figure 6, it is seen that particles of all sizes shift in Na/Cl ratio

when exposed continuously for either 5 or 15s, while only the smaller particles experience a shift when exposed repeatedly for 1s. This indicates that the local radiolysis or temperature is more severe for the continuous exposure compared to the 15 consecutive exposures, where radical concentrations and temperatures are allowed to drop between measurements.

Finally, it is seen from Figure 6 that the decrease in concentration is most severe during the first few seconds of beam exposure, highlighting the need for short EDS livetimes when working with small beam sensitive particles. This is however challenging for detectors with a relatively low solid angle, as their count rates require longer livetimes in order to reach a sufficient number of counts.

### **Quantification Method**

As discussed previously, the choice of quantification model also influences the quality of EDS results. This can be seen when comparing the FlatQuad concentrations in the top row plots of Figure 4, where beam damage is minimal. Here, the Na/Cl ratios fall directly on the 1:1 line at 20 keV, whereas the ratios at 5 keV start to deviate for higher Na and Cl concentrations, which were measured from the largest particles. The observed deviation results from the Cliff-Lorimer model, which assumes that there is minimal sample interaction. However, the lower electron energy at 5 keV shrinks the interaction volume to a depth of approximately 500 nm, compared to 4000 nm at 20 keV. As a result, the largest particles ( $D_p > D_i$ , Eq. (7)) in this study will behave as bulk samples rather than electron transparent, making P/B-ZAF better suited for quantification, though Cliff-Lorimer is still needed for the smallest sizes ( $D_p \ll D_i$ , Eq. (7)). To illustrate the difference between the two models, their Na and Cl quantification results from the 1s livetime FlatQuad measurements at 5, 10, and 20 keV (Figure 4), are plotted as Na/Cl ratios against particle size in Figure 7. Here results from the proposed interpolation model in Eq. (6) are also presented, along with the weights used for correction (scaling from 0-1).

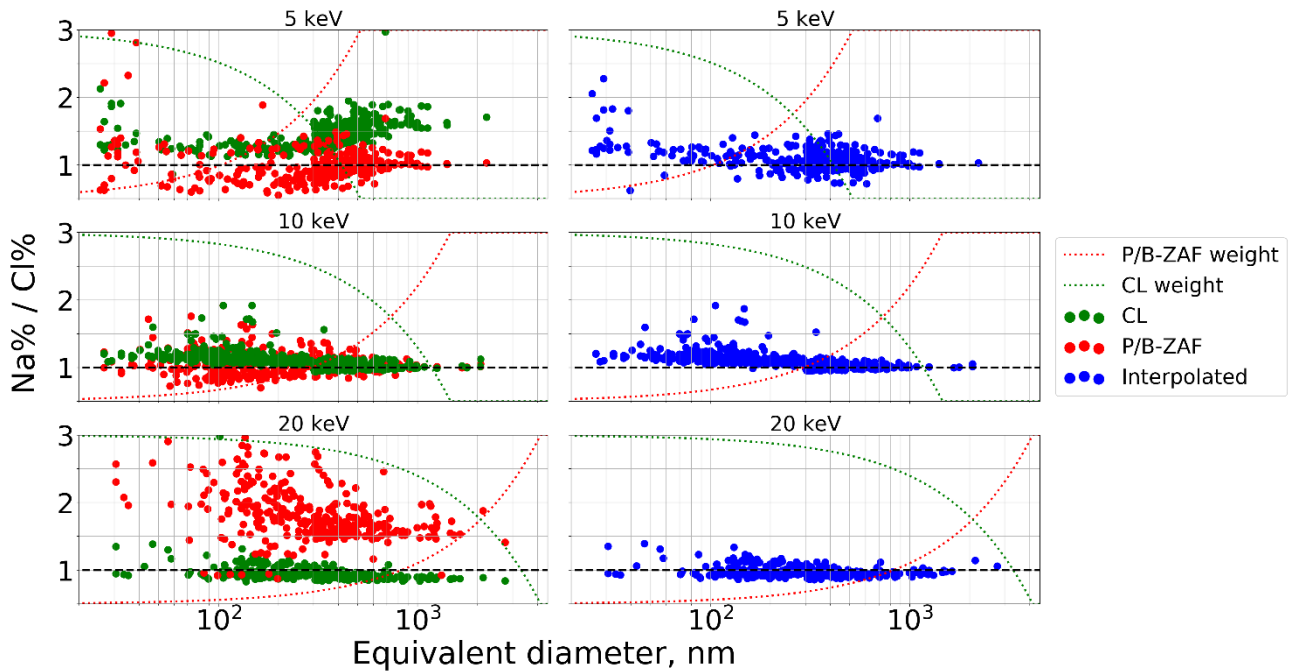


**Figure 7. Ratios of Na/Cl (at%) quantified by P/B-ZAF (red) and Cliff-Lorimer (green) plotted against particle equivalent diameter at 5 keV (top), 10 keV (middle), and 20 keV (bottom). The data points in blue are the Na/Cl ratios interpolated by the proposed algorithm in Eq. (6). The dotted red and green lines correspond to the size dependent weights of the algorithm, which scale from 0 to 1. The crossing point of the red and green dotted lines is at half the interaction depth, while the point where they reach 1 and 0 is at the interaction depth for the given voltage and density ( $2.16 \text{ g/cm}^3$  for NaCl).**

It is demonstrated that the choice of quantification model can have a significant influence on the measured concentrations. At 5 keV, the Cliff-Lorimer model slightly overestimates the Na/Cl ratios for particle sizes smaller than 200 nm, which could be the result of beam damage. However, as the particle size increase, the Cliff-Lorimer model predicts a rise in the Na/Cl ratio, resulting in values further from unity. This shows that the Cliff-Lorimer model is ill suited for quantification of the largest particle sizes, which act as bulk samples. The P/B-ZAF model reports highly varying Na/Cl ratios at small particle sizes, ranging from 0.5 to approximately 1.5. At larger sizes, the ratios converge towards unity consistent with the transition from transparent to bulk sizes, which should make the P/B-ZAF model more precise.

At 10 keV, both the Cliff-Lorimer and the P/B-ZAF models report Na/Cl ratios close to unity for all particle sizes, despite an expected discrepancy. This may however be different for samples other than NaCl, where sample interactions are different.

At 20 keV, all particle sizes are significantly smaller than the depth of the interaction volume. As a result, the P/B-ZAF model overcompensates for matrix interactions, resulting in Na/Cl ratios that are 2-3 times higher than the actual. In contrast, the Cliff-Lorimer model reports ratios close to unity for all sizes, though a systematic decrease is observed at the largest particle sizes. This indicates the

beginning of a transition from transparent to bulk sizes, which is consistent with the observations of Kandler et al. (Kandler *et al.* 2018).

Results from the proposed interpolation are shown in the plots in the right-hand side of Figure 7. At 5 keV, the interpolation presents the more precise Cliff-Lorimer ratios at small sizes, but corrects for the increase observed at larger sizes, as the P/B-ZAF model is weighted heavier. At 10 keV, both the P/B-ZAF and Cliff-Lorimer ratios are close to unity at all sizes and the interpolation therefore resembles both. At 20 keV, all particles are significantly smaller than the interaction volume, and the interpolation is largely based on the Cliff-Lorimer results. However, it is seen that the interpolation corrects for the slight decrease in the Cliff-Lorimer ratios at larger sizes, by introducing the weighted P/B-ZAF results. Finally, it is seen that some degree of beam damage is observed for the smallest particle sizes, where all of the interpolated values are slightly above unity. This effect is again most severe at 5 keV and least so at 20 keV, consistent with the observations in Figure 4. Overall, the Na/Cl ratios determined with the interpolation are close to unity for all particle sizes and all acceleration voltages used in this study. Additional research is however needed to investigate its use for larger particle sizes, and for samples other than NaCl, potentially with different shapes.

### **Comparison of Mapping and Feature analysis**

The increased count rate and the following decrease in acquisition time achievable with the FlatQuad detector, opens the possibility for using mapping as opposed to feature analysis. Here the two techniques are compared and their advantages and disadvantages are discussed.

#### *Feature analysis*

Feature analysis can greatly reduce the time needed to perform EDS analysis, as only pixels recognized as particles are taken into account. The majority of the image (all pixels not recognized as particles) is thus excluded from the analysis. This is a major advantage when using low solid angle detectors that require a long exposure time to reach sufficient X-ray counts. Feature analysis also makes it possible to set a fixed EDS livetime per particle, set a minimum number of X-ray counts needed per particle, or set a fixed pixel dwelltime. Minimum count requirements can be used to ensure sufficient X-ray counts from particles of all sizes or composition, while a fixed pixel dwelltime can be used to minimize beam damage for sensitive samples. However, the image segmentation can be difficult and often yields poor results, especially when automated imaging is used for analysis of multiple areas or images in sequence. A poor segmentation can result in a large number of substrate areas misclassified as particles, which increases the overall analysis time extensively, and in worst case require the automated analysis to be aborted or discarded. A new image segmentation can be made in case of poor results, but as the EDS analysis was limited to the predetermined pixels, the new segmentation can only give physical parameters and not composition. Feature analysis also has significant weaknesses, when sample drift is not accounted for (e.g. by drift correction). Since image segmentation is performed prior to EDS analysis, sample drift can cause the beam to completely or partially miss targeted particles, or mix EDS results from a neighboring area into the segmented particle, which is not apparent for the user. It can be very challenging to determine

whether drift occurred during the analysis, unless SE images are acquired both before and after analysis and compared, and even then, charging differences may make this irreproducible. Ultimately, the entire analysis may need to be repeated, which can be an issue for beam sensitive samples, as the previous SEM/EDS analysis may have altered the shape or composition of already analyzed particles, hence requiring a new sample area.

### *Mapping*

Mapping generally takes longer to perform compared to feature analysis, as all pixels are included in the EDS analysis. Furthermore, it is only possible to use fixed pixel dwelltimes, as particles are not yet distinguished from the substrate. This results in very low beam exposure for small particles, making their determined elemental compositions highly uncertain. However, unlike feature analysis, mapping allows for offline image segmentation, since both SE and EDS signals are stored individually for all pixels. This opens up for multiple post processing options, such as segmentation based not only on the SE image, but also on elemental maps generated from EDS data. Images and individual particles can therefore be visually screened for specific elements of interest. Additionally, the element distributions available in maps provide information on the heterogeneity in the mixing state of individual particles. This information is highly useful when classifying particles, since primary particles of different composition are easily distinguished in EDS, even if they exist in agglomerated forms, consisting of several different primary particles. Finally, mapping makes it possible to subtract the EDS contribution originating from the sample substrate, from each individual particle, as will be demonstrated later.

### *Dwelltime and Livetime comparison*

For a fixed pixel dwelltime, small particles consisting of only a few pixels will have very low beam exposure, yielding low X-ray counts. This is exemplified in Figure 8, where the Na X-ray count of individual particles are plotted against their area in pixels, for particles analyzed by feature analysis with 1s livetime and for four maps with a pixel dwelltime of 64, 128, 256, and 512  $\mu\text{s}/\text{pixel}$ , respectively. Each analysis was performed in different areas of the sample to avoid beam damage. The acquisition times of the maps were approximately 4, 7.5, 15, and 30 minutes, respectively, while the feature analysis was completed in approximately 3 minutes with 142 particles in total (and some deadtime in between particles).

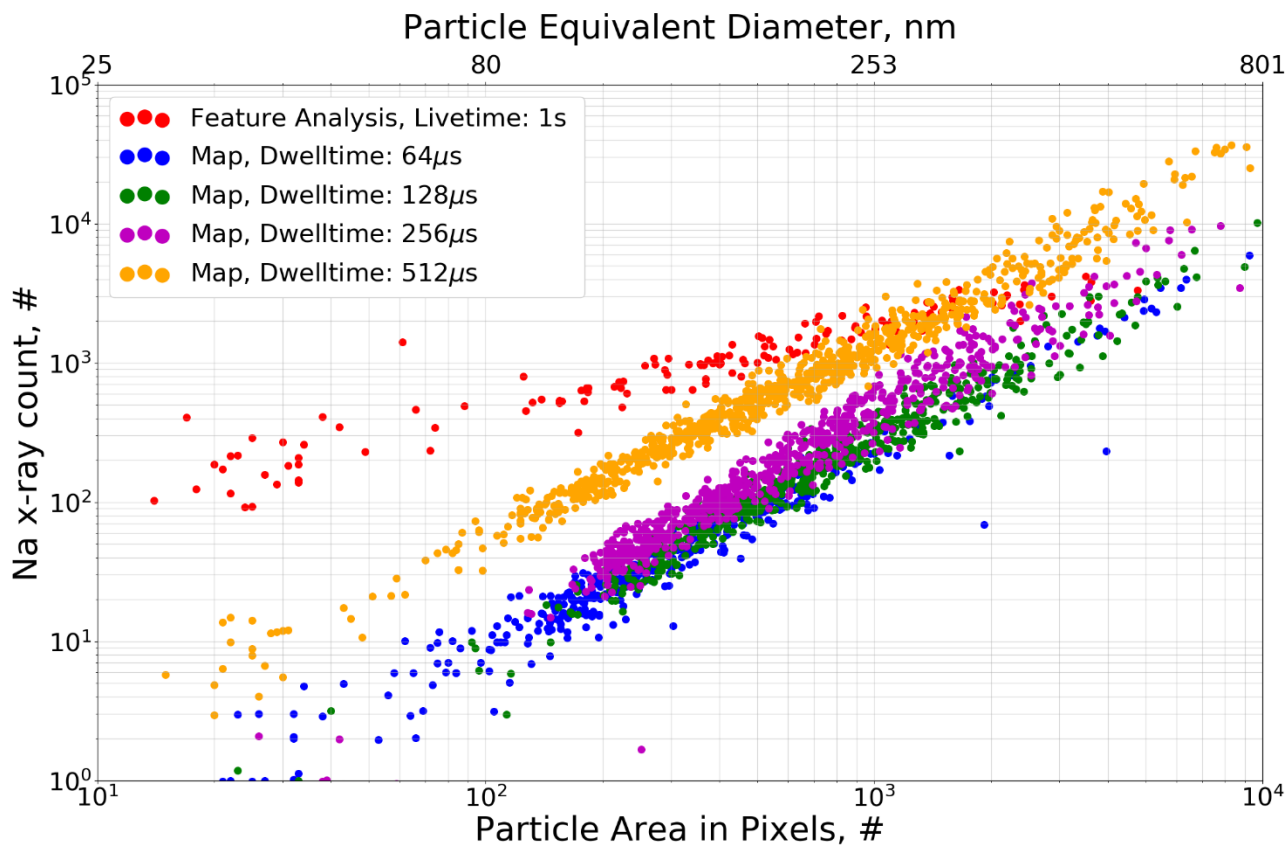


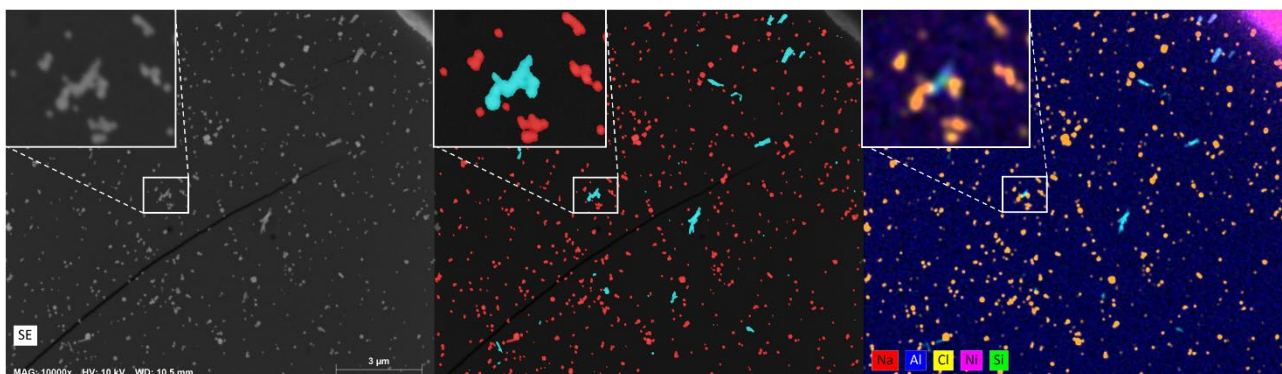
**Figure 8. Total X-ray count in the Na peak for individual particle EDS spectra after bremsstrahlung background subtraction for a feature analysis with 1s livetime and four EDS maps with pixel dwelltimes of 64, 128, 256, and 512  $\mu$ s. Particle sizes are displayed as area in pixels on the bottom x-axis and as equivalent circular diameters in nm in the top x-axis, both in logarithmic scale. All analyses were performed at 10 keV and at 10k magnification, corresponding to a pixel size of 7.1 nm.**

It is seen in Figure 8 that the X-ray count in the Na peaks is much higher for small particles when using feature analysis with a fixed particle livetime, compared to the fixed pixel dwelltime applied in mapping. This is because the overall exposure time is fixed for feature analysis but decreases with size for mapping. The particle X-ray yield in mapping is therefore highly particle size dependent, while size is less significant for fixed livetimes where all particles are exposed for the same amount of time. However, the X-ray yield with fixed livetimes is still influenced by the particle volume, which determines the fraction of incoming electrons that interact with the particle (assuming the same elemental composition). Since volume is roughly proportional to area, the fixed livetime X-ray yield still has some size dependency. This is particularly evident at small sizes where many electrons are transmitted, while it is insignificant for larger sizes where the majority of the interaction volume is within the particle. If this volume dependency is ignored, the particle size where mapping yields higher counts than fixed livetimes can be calculated, as presented in the SI. For a feature analysis with 1s livetime the crossing points are at particle sizes of approximately 15600, 7800, 3900, and 1950 pixels for map dwelltimes of 64, 128, 256, and 512  $\mu$ s, respectively. For the images presented

here, which have a pixel resolution of 7.1 nm/pixel, these sizes correspond to equivalent circular diameters of approximately 1000, 700, 500, and 350 nm, for the four dwelltimes respectively. The particle sizes at the crossing points can be reduced by performing the map analysis at higher magnification, thereby increasing the number of pixels within each particle. This will however reduce the area covered in each image and thereby increase the overall analysis time if the same area is to be analyzed. This shows that the feature analysis with a fixed livetime is better suited for EDS analysis of small particles compared to maps with a fixed pixel dwelltime. It should however be noted that the smaller particles are more sensitive to sample drift and subject to intense beam radiation for fixed livetimes, and the method is therefore less suited for beam sensitive samples.

### *Classification of particles*

The individual pixel data in maps enables visualization of the internal particle mixing state, as opposed to the integrated elemental composition obtained by feature analysis. Interpreting the visualized data from elemental maps makes it possible to distinguish fully mixed particles from aggregates and agglomerates. An area on the NaCl sample contained trace contamination by aluminosilicate particles from an earlier experiment in the aerosol system. An SE image from this area is shown in Figure 9 (left), along with the results from a feature analysis, where particles were classified based on their elemental composition (middle), as well as an overlay of element maps (right). The overlaying element maps show X-ray counts of various elements, which have been normalized so that the highest count corresponds to a pixel intensity of 255.



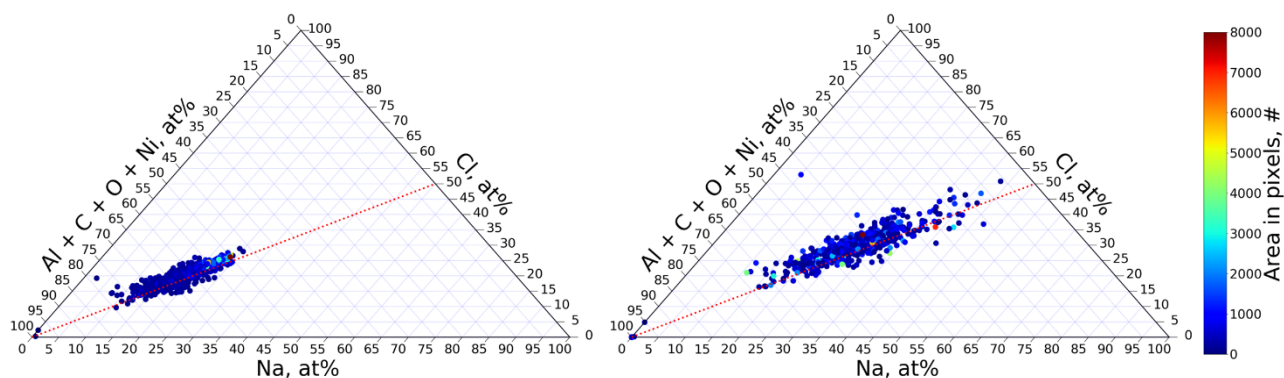
**Figure 9. Left: SE image of an area of the NaCl sample contaminated with aluminosilicate particles. Middle: Classified image from a feature analysis with a livetime of 1s, where particles with Na+Cl at% higher than 4 are shown in red, while particles with Si at% higher than 2 are cyan (overwriting the Na+Cl criteria). Right: Overlaying element maps displaying X-ray counts for Na(red), Al(blue), Cl(yellow), Ni(magenta), and Si(green). The maps were acquired with a pixel dwelltime of 256 μs. Inserts depict a zoom in on the same agglomerate particle consisting of NaCl particles and an aluminosilicate fiber.**

Figure 9 shows that much more detail is available from the map compared to the classified image. Overlay of the red Na and the yellow Cl maps yield orange particles, corresponding to NaCl crystals, which, as expected, are fully mixed. A vague blue color covers the entire image, which originates from the Al background signal generated when transmitted or stray electrons hit the sample holder

or other stage parts of the microscope. A similar effect would be seen if the element maps for carbon and oxygen had been included, as they are the main components of the Formvar substrate. Cyan colored particles are also observed, originating from overlay of green silicon and blue aluminum maps, consistent with the presence of aluminosilicate particles. The map furthermore enables visualization of the mixing state of particles. Hence, the cyan colored particle near the center of the classified image, and highlighted in the insert, reveals that an aluminosilicate particle has coagulated with several smaller NaCl particles. In contrast, the feature analysis shows only an integrated particle composition, and can therefore not distinguish the four primary particles. The knowledge of particle mixing state can be highly useful for identification of particle sources in complex atmospheric aerosols. Additionally, maps can be analyzed offline, yielding tables with physical and elemental composition results for each individual particle similar to that obtained by feature analysis. Maps can therefore produce the same results as feature analysis, while providing supplementary information on individual particle mixing state.

#### *Subtraction of substrate EDS contribution*

Mapping furthermore makes it possible to subtract the substrate/background contribution from individual particle EDS spectra. This is done by determining the mean X-ray count for each element per pixel in the image area recognized as substrate and subsequently subtracting it from the individual particle X-ray spectra, taking into account the varying particle size. The substrate subtraction will highly influence small particles, with a substantial contribution from the substrate, but less so for larger particles. It may be necessary to set negative X-ray counts to zero, in case the substrate contribution is overestimated. Afterwards, the X-ray counts can be converted to mass% via Eq. (5) and to at% if needed. Figure 10 shows examples of substrate subtraction made by segmenting an SE image into two phases: a particle phase, containing all pixels with intensities above a set threshold value; and a substrate phase consisting of all pixels with an intensity below a given threshold. The resulting phase-separated image can be seen in the SI. The mean substrate pixel X-ray count for all elements were determined from the size and spectrum of the substrate phase, which was subtracted from the individual particle spectra after multiplying with the given particle size in pixels.



**Figure 10. Ternary plots of at% for Na, Cl, and the sum of all other detected elements, determined from a map acquired at 10 keV with a dwelltime of 512  $\mu\text{s}/\text{pixel}$ . Left: Plot of particle EDS data**

**without substrate subtraction. Right: Plot of particle EDS data with substrate subtraction. Data points are colored according to particle area in pixels, displayed on the colorbar. The 1:1 line for the Na/Cl at% ratio is plotted as a red dotted line.**

Before substrate subtraction the measured Na + Cl concentration vary from approximately 20 to 50 at% for all NaCl particles, while the remaining concentration is made up of C, O, Ni, or Al, originating from the substrate or inside of the microscope (left plot in Figure 11). It is furthermore seen that the Na + Cl content increase with particle size, with the highest concentrations found for the largest particles, as less electrons are transmitted. After substrate subtraction (right plot in Figure 11), the data points are shifted along the 1:1 line of the Na/Cl ratio, showing that the procedure can distinguish and remove contributions from substrate and microscope, while maintaining particle element ratios of Na and Cl. The resulting Na + Cl concentrations range from approximately 30 to 90 at%, hence approaching pure NaCl particles. It is furthermore seen that the size dependency has disappeared, as the substrate contributions for small particles have been significantly reduced. This allows for high Na + Cl concentrations even for small particles with limited X-ray counts. Substrate subtraction can hence be a useful tool when analyzing small particles, where significant contributions from substrate and microscope are an issue. However, the method will need additional testing, especially when analyzing particles consisting of elements, which are present in the background spectrum. It may also be necessary to introduce size weights, which corrects for the decreasing background contribution with increasing particle sizes.

The discussed advantages and disadvantages between using feature analysis and mapping are summarized in Table 2.

**Table 2. Overview of the discussed advantages and disadvantages between feature analysis and EDS mapping as analysis strategies for characterization of single particles.**

	<b>Feature analysis</b>	<b>Mapping</b>
<b>EDS scan setting</b>	Livetime, dwelltime, minimum X-ray count	Dwelltime
<b>Overall analysis time</b>	Depends on setting (shorter)	Constant (longer)
<b>X-ray count small particles</b>	Depends on setting	Low
<b>X-ray count large particles</b>	Depends on setting	High
<b>Drift sensitive</b>	Yes	No
<b>Segmentation</b>	Online	Offline
<b>Revise segmentation</b>	No	Yes
<b>Element segmentation</b>	No	Yes
<b>Particle mixing state</b>	No	Yes
<b>Substrate subtraction</b>	No	Yes

## Conclusion

The SEM/EDS analysis of electron transparent beam sensitive NaCl particles was performed with two types of EDS detectors for comparison, namely the XFlash 6|30, 30 mm<sup>2</sup> SDD, representing

traditional SDD detectors, and the newly developed annular FlatQuad 4x15 mm<sup>2</sup> SDD detector. In this study the annular detector was found to have a superior count rate, allowing a significant reduction in EDS acquisition time, while ensuring a counting statistics uncertainty below or close to 2%, even for 1s particle livetimes. For feature analysis an EDS livetime of 1s was found optimal for minimizing beam damage of NaCl particles, as it resulted in Na/Cl ratios close to 1 for all acceleration voltages. Longer livetimes resulted in enrichment of Na relative to Cl, indicating beam damage consistent with mechanisms reported in the literature. Here it was also seen that beam damage was most severe at 5 keV, while the higher degree of transmitted electrons at 20 keV, resulted in less. It is therefore recommended to use 20 keV, when analyzing beam sensitive samples.

Ratios of Na/Cl were compared when quantifying with Cliff-Lorimer or P/B-ZAF. As expected, the P/B-ZAF model was optimal at larger and bulk sizes, though it overcompensated for matrix effects for smaller particle sizes. This was especially obvious at 20 keV, where the P/B-ZAF model overestimated Na/Cl ratios by a factor of 2-3 for all particle sizes used in this study. The Cliff-Lorimer model was found suited for thin samples, though it over predicted Na/Cl ratios of particles larger than 300 nm at 5 keV. This shows that the transition from transparent to bulk sizes depends on acceleration voltage. The ratio between particle size and electron interaction depth was therefore tested to determine if it could be used as a weight to interpolate results from the two quantification models. The interpolation provided consistent results close to 1 for all particle sizes at all acceleration voltages used in this study. Additional research is needed to confirm its use for larger particle sizes and for particles other than NaCl and potentially those with more complex shapes.

Finally, a comparison was made between EDS mapping and feature analysis, as mapping was found to be a viable option due to the increased count rates obtainable with the annular detector. The advantages and disadvantages of the two methods are summarized in Table 2, where especially offline and additional segmentation options as well as the higher degree of detail are noteworthy advantages for mapping. Overall, it was shown that the recent advances in EDS detectors allow for detailed sample information on a very short timescale, which enables accurate analysis of nanoparticles and beam sensitive samples, and makes SEM/EDS analysis more applicable in a broad range of scientific fields.

## **Acknowledgements**

The authors acknowledge the Danish Centre for NanoSafety II at the National Research Centre for the Working Environment and the National Centre for Nano Fabrication and Characterization, Technical University of Denmark (DTU) for supporting this PhD-study. The authors also acknowledge Bruker Nano and especially Daniel Goran, for assisting with detector parameters and descriptions, as well as feedback on the final manuscript.

## **References**

- Allen, H. C., Mecartney, M. L., & Hemminger, J. C. (1998). Minimizing transmission electron microscopy beam damage during the study of surface reactions on sodium chloride. *Microscopy and Microanalysis*, **4**(1), 23–33.

- Arepalli, S., Nikolaev, P., Gorelik, O., ... Yowell, L. (2004). Protocol for the characterization of single-wall carbon nanotube material quality. *Carbon*, **42**(8–9), 1783–1791.
- Armstrong, J. T., & Buseck, P. R. (1975). Quantitative Chemical Analysis of Individual Microparticles using the eElectron Microprobe: Theoretical. *Analytical Chemistry*, **47**(13), 2178–2192.
- Brodusch, N., Demers, H., & Gauvin, R. (2018). Chapter 7: X-ray imaging with a silicon drift detector energy dispersive spectrometer. In *SpringerBriefs in Applied Sciences and Technology*, pp. 67–84.
- Brostrøm, A., Kling, K. I., Koponen, I. K., Hougaard, K. S., Kandler, K., & Mølhav, K. (2019). Improving the foundation for particulate matter risk assessment by individual nanoparticle statistics from electron microscopy analysis. *Scientific Reports*, **9**(1), 8093.
- Cazaux, J. (1995). Correlations between ionization radiation damage and charging effects in transmission electron microscopy. *Ultramicroscopy*, **60**(3), 411–425.
- Cliff, G., & Lorimer, G. W. (1975). The quantitative analysis of thin specimens. *Journal of Microscopy*, **103**(2), 203–207.
- Demers, H., Poirier-Demers, N., Couture, A. R., ... Drouin, D. (2011). Three-dimensional electron microscopy simulation with the CASINO Monte Carlo software. *Scanning*, **33**(3), 135–146.
- Duncumb, P., & Reed, S. J. B. (1968). The calculation of stopping power and backscatter effects in electron probe microanalysis. *Quantitative Electron Probe Microanalysis*, (298), 133–154.
- Egerton, R. F., Li, P., & Malac, M. (2004). Radiation damage in the TEM and SEM. *Micron*, **35**(6), 399–409.
- Fletcher, R. A., Ritchie, N. W. M., Anderson, I. M., & Small, J. A. (2011). Microscopy and Microanalysis of Individual Collected Particles. *Aerosol Measurement: Principles, Techniques, and Applications: Third Edition*, 179–232.
- Friel, J. J., & Lyman, C. E. (2006). X-ray Mapping in Electron-Beam Instruments. *Microscopy and Microanalysis*, **12**, 2–25.
- Hovington, P., Timoshevskii, V., Burgess, S., ... Zaghbi, K. (2016). Can we detect Li K X-ray in lithium compounds using energy dispersive spectroscopy? *Scanning*, **38**(6), 571–578.
- Kandler, K., Schneiders, K., Ebert, M., ... Pöhlker, C. (2018). Composition and mixing state of atmospheric aerosols determined by electron microscopy: Method development and application to aged Saharan dust deposition in the Caribbean boundary layer. *Atmospheric Chemistry and Physics*, **18**(18), 13429–13455.
- Kandler, K., Schütz, L., Deutscher, C., ... Weinbruch, S. (2009). Size distribution, mass concentration, chemical and mineralogical composition and derived optical parameters of the boundary layer aerosol at Tinfou, Morocco, during SAMUM 2006. *Tellus, Series B: Chemical and Physical Meteorology*, **61**(1), 32–50.
- Kling, K. I., Levin, M., Jensen, A. C. Ø., Jensen, K. A., & Koponen, I. K. (2016). Size-resolved characterization

of particles and fibers released during abrasion of fiber-reinforced composite in a workplace influenced by ambient background sources. *Aerosol and Air Quality Research*, **16**(1), 11–24.

- Koh, A. L., Shachaf, C. M., Elchuri, S., Nolan, G. P., & Sinclair, R. (2008). Electron microscopy localization and characterization of functionalized composite organic-inorganic SERS nanoparticles on leukemia cells. *Ultramicroscopy*, **109**(1), 111–121.
- Laskin, A., & Cowin, J. P. (2001). Automated single-particle SEM/EDX analysis of submicrometer particles down to 0.1  $\mu\text{m}$ . *Analytical Chemistry*, **73**(5), 1023–1029.
- Laskin, A., Cowin, J. P., & Iedema, M. J. (2006). Analysis of individual environmental particles using modern methods of electron microscopy and X-ray microanalysis. *Journal of Electron Spectroscopy and Related Phenomena*, **150**(2–3), 260–274.
- Lee, J. S., Choi, Y. C., Shin, J. H., ... Yu, I. J. (2015). Health surveillance study of workers who manufacture multi-walled carbon nanotubes. *Nanotoxicology*, **9**(6), 802–811.
- Lee, K. M., Cai, Z., Griggs, J. A., Guistas, L., Lee, D. J., & Okabe, T. (2004). SEM/EDS Evaluation of Porcelain Adherence to Gold-Coated Cast Titanium. *Journal of Biomedical Materials Research - Part B Applied Biomaterials*, **68**(2), 165–173.
- Newbury, D. E., & Ritchie, N. W. M. (2013). Is scanning electron microscopy/energy dispersive X-ray spectrometry (SEM/EDS) quantitative? *Scanning*, **35**(3), 141–168.
- Newbury, D. E., & Ritchie, N. W. M. (2014). Performing elemental microanalysis with high accuracy and high precision by scanning electron microscopy/silicon drift detector energy-dispersive X-ray spectrometry (SEM/SDD-EDS). *Journal of Materials Science*, **50**(2), 493–518.
- PHILIBERT, J. (1963). A Method for Calculating the Absorption Correction in Electron-Probe Microanalysis. *X-Ray Optics and X-Ray Microanalysis*, 379–392.
- Potts, P. J. (1987). A Handbook of Silicate Rock Analysis. In *A Handbook of Silicate Rock Analysis.*, p. 336.
- Reed, S. J. B. (1965). Characteristic fluorescence corrections in electron-probe microanalysis. *British Journal of Applied Physics*, **16**(7), 913–926.
- Ro, C. U., Osán, J., Szalóki, I., De Hoog, J., Worobiec, A., & Van Grieken, R. (2003). A Monte Carlo program for quantitative electron-induced X-ray analysis of individual particles. *Analytical Chemistry*, **75**(4), 851–859.
- Sathirachinda, N., Pettersson, R., Wessman, S., & Pan, J. (2010). Study of nobility of chromium nitrides in isothermally aged duplex stainless steels by using SKPFM and SEM/EDS. *Corrosion Science*, **52**(1), 179–186.
- Stebounova, L. V., Adamcakova-Dodd, A., Kim, J. S., ... Thorne, P. S. (2011). Nanosilver induces minimal lung toxicity or inflammation in a subacute murine inhalation model. *Particle and Fibre Toxicology*, **8**. doi:10.1186/1743-8977-8-5

- Teng, C., Demers, H., Brodusch, N., Waters, K., & Gauvin, R. (2018). Use of an Annular Silicon Drift Detector (SDD) Versus a Conventional SDD Makes Phase Mapping a Practical Solution for Rare Earth Mineral Characterization. *Microscopy and Microanalysis*, **24**(3), 238–248.
- Watanabe, M., & Williams, D. B. (2006). *The quantitative analysis of thin specimens: A review of progress from the Cliff-Lorimer to the new  $\zeta$ -factor methods*. *Journal of Microscopy*, Vol. 221.
- Wendt, M. (1978). Advances in energy dispersive X-ray microanalysis. *Kristall und Technik*, **13**(11), 1259–1275.
- Wendt, M., & Schmidt, A. (1978). Improved reproducibility of energy-dispersive X-ray microanalysis by normalization to the background. *Physica Status Solidi (A)*, **46**(1), 179–183.

## Supporting Information for:

# Analysis of Electron Transparent Beam Sensitive Samples using Scanning Electron Microscopy coupled with Energy Dispersive X-ray Spectroscopy

Anders Brostrøm<sup>1,2</sup>, Kirsten Inga Kling<sup>3</sup>, Karin Sørig Hougaard<sup>2</sup>, and Kristian Mølhave<sup>1\*</sup>

<sup>1</sup>Technical University of Denmark, DTU Nanolab – National Centre for Nano Fabrication and Characterization, Fysikvej, Building 307, 2800 Kgs Lyngby, Denmark

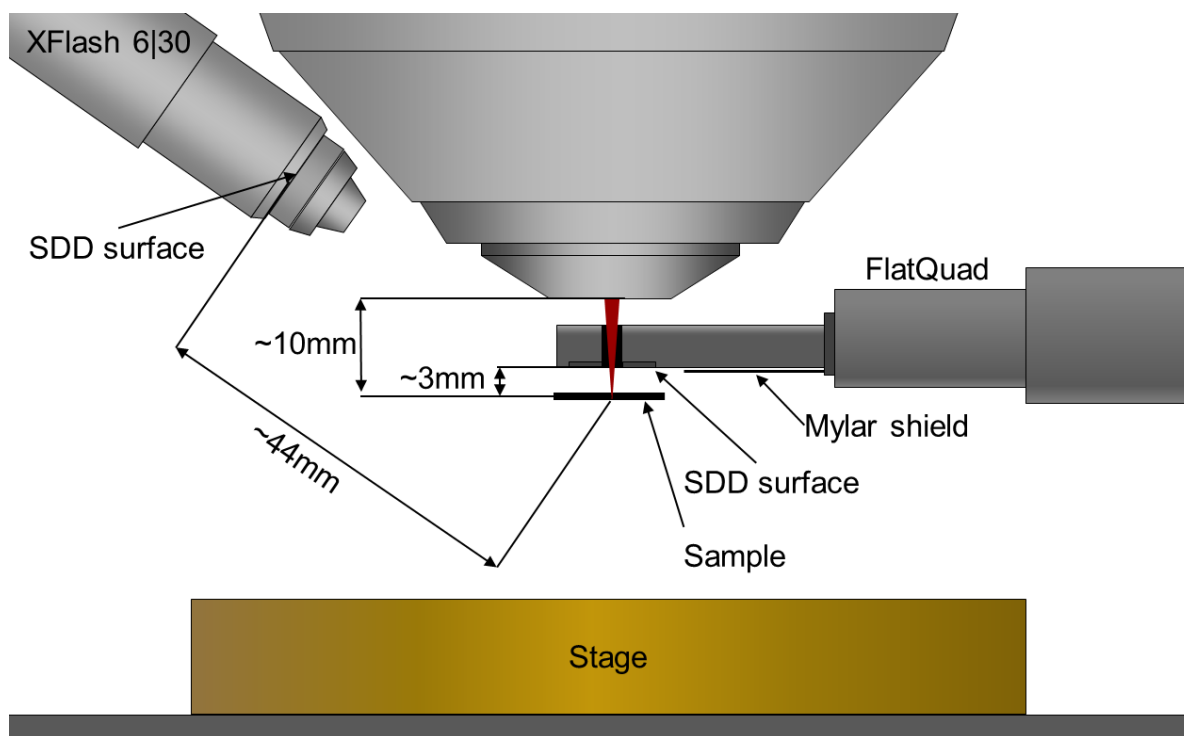
<sup>2</sup>National Research Centre for the Working Environment, Lersø Parkallé 105, 2100 Copenhagen, Denmark

<sup>3</sup>Technical University of Denmark, DTU Nanolab – National Centre for Nano Fabrication and Characterization, Fysikvej, Building 347, 2800 Kgs Lyngby, Denmark

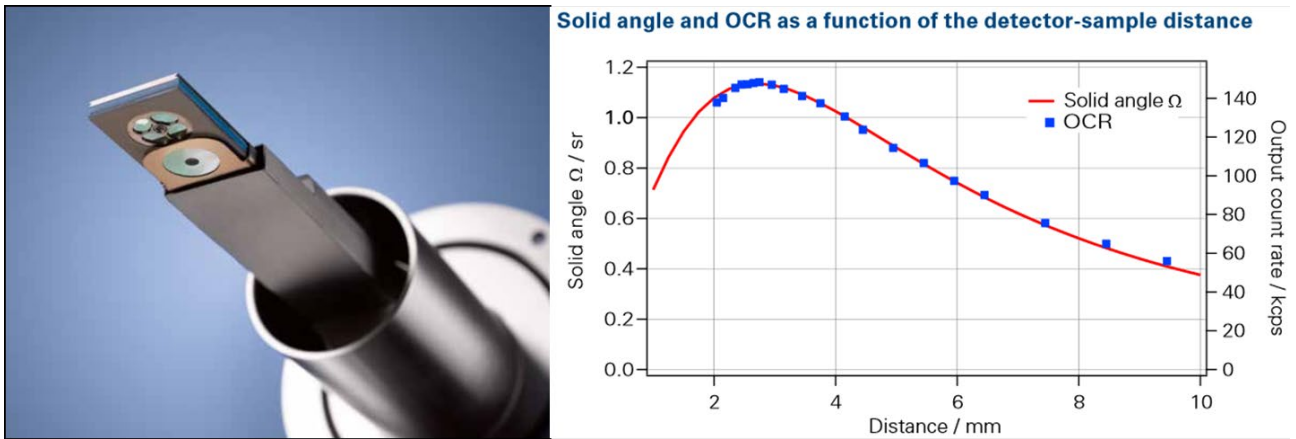
\*Corresponding author: krmo@dtu.dk

## Microscope configuration

A sketch of the detector configurations inside the SEM is shown in SI Figure 1. The FlatQuad detector was retracted when performing EDS measurements with the XFlash detector, as it would otherwise block a large fraction of the generated X-rays.



SI Figure 1. Schematic overview of EDS detector setup in the microscope.



SI Figure 2. Left: Image of the bottom of the FlatQuad detector, showing the four SDD quadrants and the retractable Mylar shield. Right: Plot of the theoretically calculated solid angle of the FlatQuad detector and measured output count rate (OCR) against the sample-detector distance, showing the optimal count rate at a distance of approximately 3 mm. The solid angles were calculated according to Nestor J. Zaluzec, Detector Solid Angle Formulas for Use in EDS, *Microsc. Microanal.* 15 (2009), 93. Images reprinted with permission, from QUANTAX FlatQUAD Brochure, Bruker Nano GmbH, Berlin, Germany.

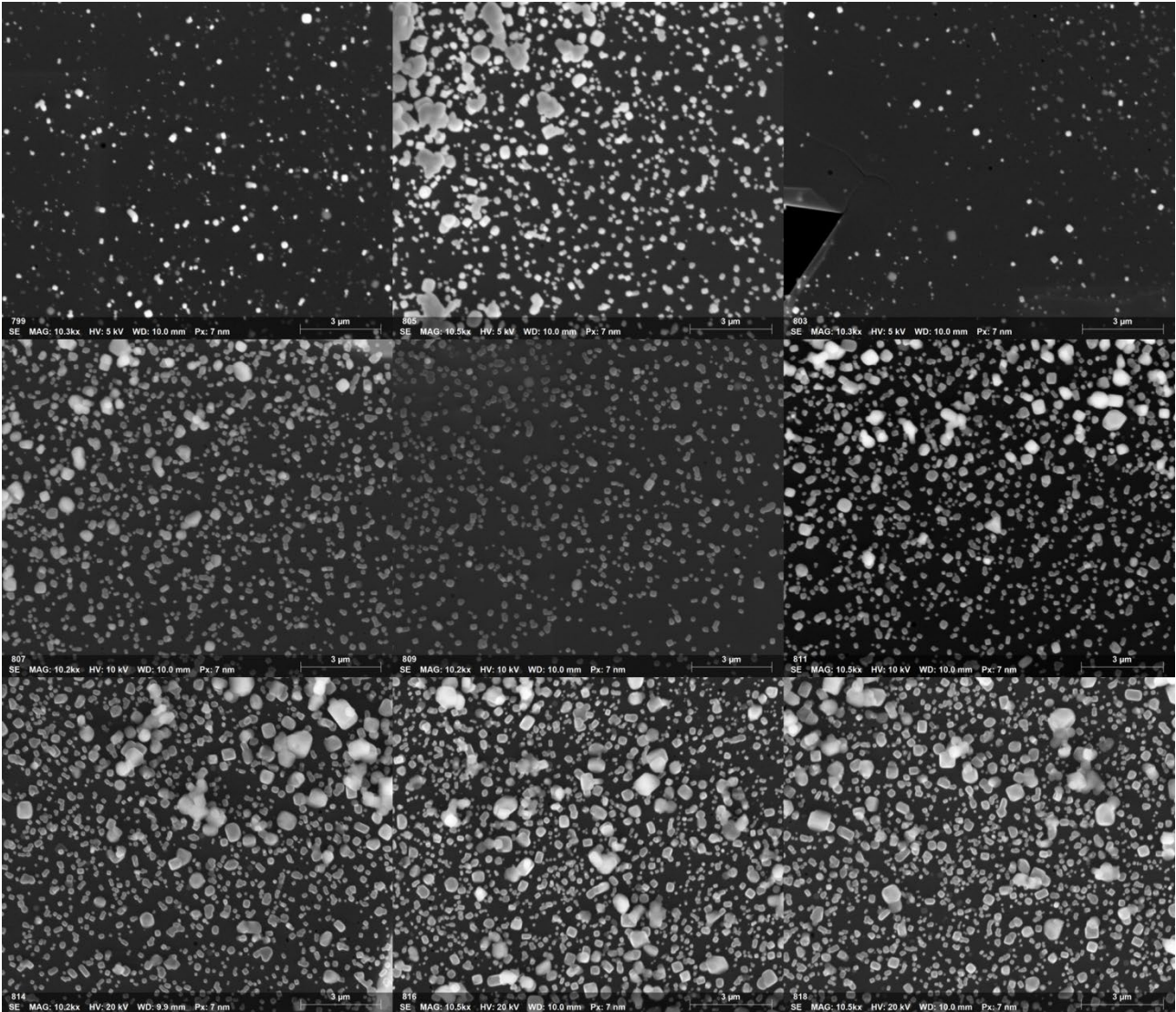
## Overview of Analyses

In this section an overview is presented of the different microscope software and hardware settings used when analyzing the NaCl sample. Furthermore the 9 different images used for feature analysis with the XFlash EDS detector are shown.

SI Table 1. Overview of microscope settings for the EDS feature analyses, using either the XFlash or FlatQuad EDS detectors.

Image Number, #	Livetime, s	Acceleration Voltage, keV	Detector
1	1	5	XFlash
2	5	5	XFlash
3	15	5	XFlash
4	1	10	XFlash
5	5	10	XFlash
6	15	10	XFlash
7	1	20	XFlash
8	5	20	XFlash
9	15	20	XFlash
10	1	5	FlatQuad
11	5	5	FlatQuad
12	15	5	FlatQuad
13	1	10	FlatQuad
14	5	10	FlatQuad

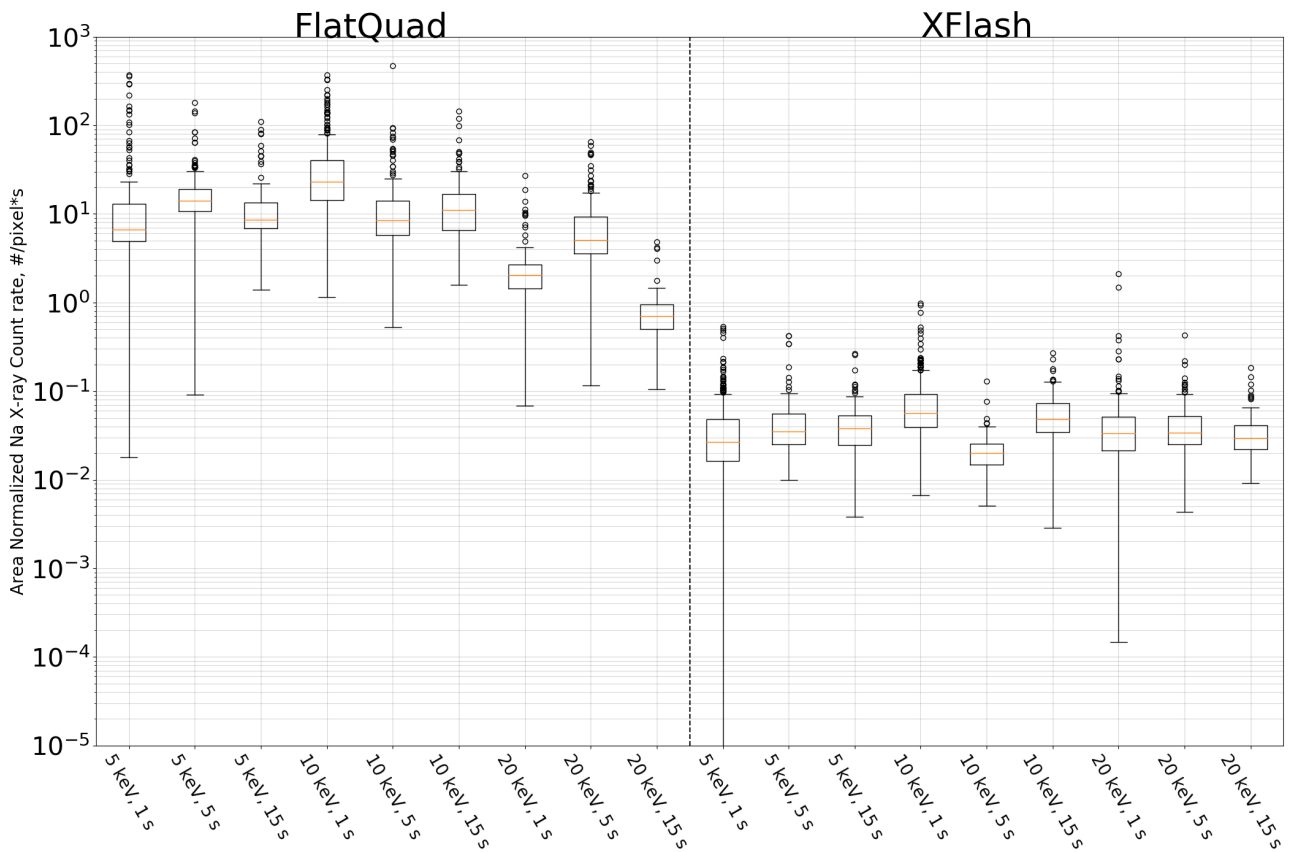
15	15	10	FlatQuad
16	1	20	FlatQuad
17	5	20	FlatQuad
18	15	20	FlatQuad



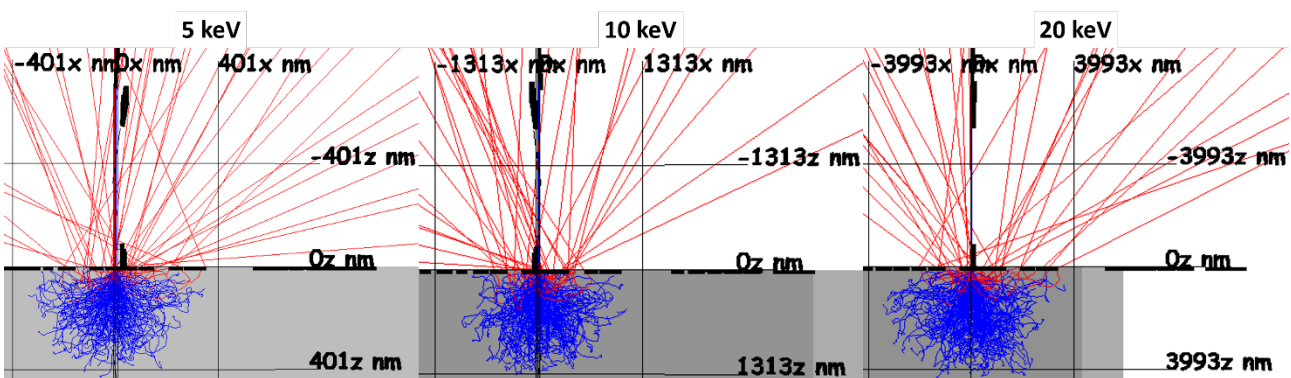
SI Figure 3. The 9 images used for feature analysis with the XFlash detector, with image 1 (from SI Table 1) in the upper left corner and image 9 in the lower right corner. For feature analysis the images were segmented with a global threshold and particles touching the edge of the image were discarded.

SI Table 2. Overview of acceleration voltages, livetimes, and particle sizes for the spectra in Figure 2 in the paper, using the two detectors. In addition, the total X-ray count in each spectrum from 100 eV to the incident beam energy is listed.

Detector	Acceleration Voltage, keV	Livetime, s	$D_{eq}$ , nm	Total X-ray count, #
FlatQuad	5	1	126	$2.6 * 10^4$
	5	1	563	$13.8 * 10^4$
	10	1	93	$3.9 * 10^4$
	10	1	502	$16.4 * 10^4$
	20	1	134	$4.5 * 10^4$
	20	1	505	$19.0 * 10^4$
	5	15	129	$42.7 * 10^4$
	5	15	490	$96.9 * 10^4$
	10	15	95	$40.2 * 10^4$
	10	15	444	$112.0 * 10^4$
	20	15	117	$43.4 * 10^4$
	20	15	418	$95.4 * 10^4$
	XFlash	5	1	94
5		1	431	184
10		1	134	238
10		1	546	540
20		1	101	11
20		1	567	403
5		15	108	659
5		15	290	2193
10		15	101	1504
10		15	453	7515
20		15	131	912
20		15	515	5416



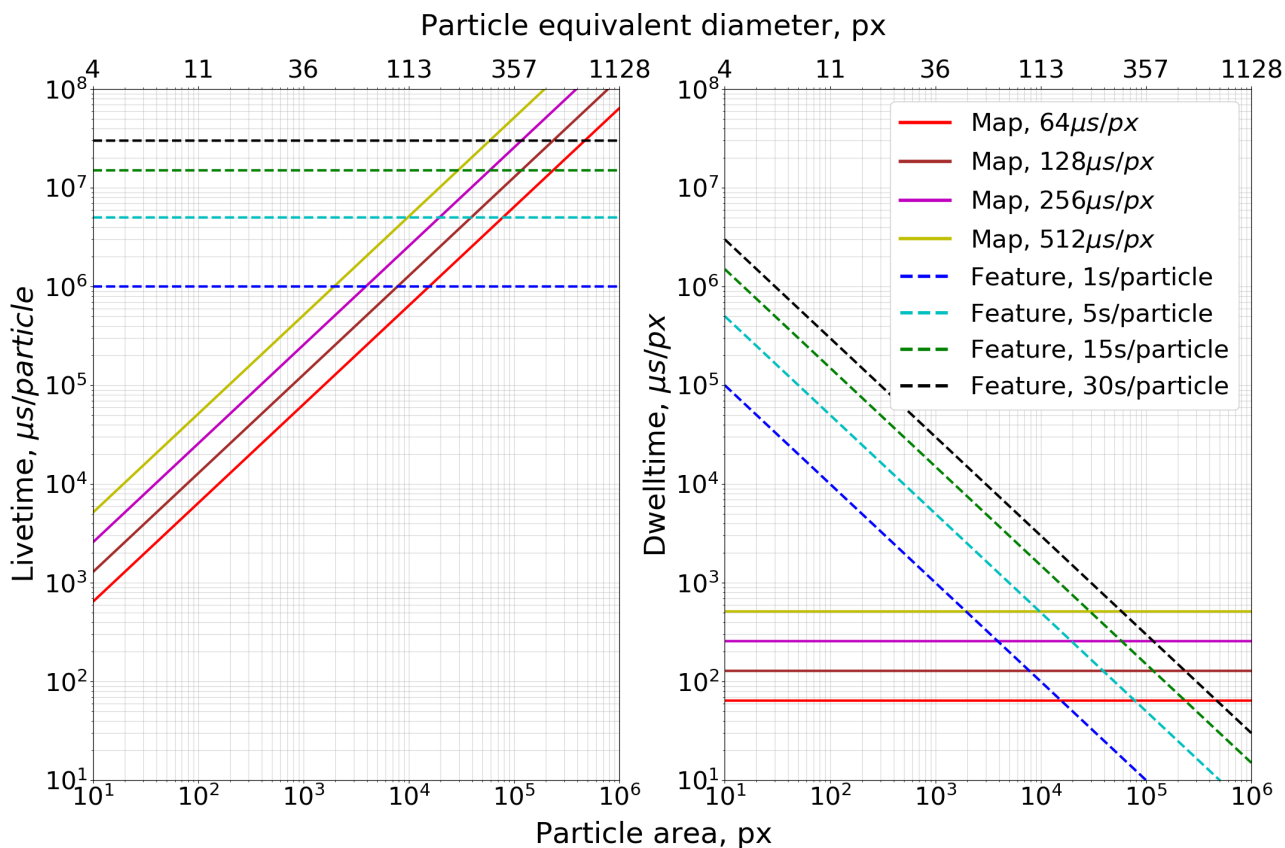
SI Figure 4. Boxplot showing the median and percentiles of the area and livetime normalized Na X-ray counts for all microscope settings with both detectors.



SI Figure 5. Images of simulated electron trajectories, performed with the Monte Carlo simulation software Casino v.3.3. Simulations were made for 10000 trajectories at 5 (left), 10 (middle), and 20 keV (right), with an incident beam diameter of 5 nm. The grey area represents a bulk NaCl crystal. The blue lines are electron trajectories occurring inside the bulk NaCl, while red lines correspond to backscattered electrons. It should be noted that the scales are different on the three simulations.

### Dwelltime and Livetime comparison

A comparison of beam exposure per particle for various particle sizes, when setting either a fixed livetime (feature analysis) or fixed dwelltime (mapping) is presented in the left plot of SI Figure 4. Alternatively, the beam exposure per pixel for various particle sizes, when setting either a fixed livetime or dwelltime is presented on the right.



SI Figure 6. A comparison of livetimes (left) and dwelltimes (right) as a function of particle size, for different map and feature analysis settings. Particle sizes are displayed as area in pixels in the bottom x-axis and as particle equivalent circular diameter in pixels on the top x-axis.

From the livetime plot on the left it is seen that the beam exposure and therefore also X-ray yield for particles consisting of only a few pixels, is orders of magnitudes lower for maps compared to feature analysis with a fixed livetime. However, as the particle sizes increase the map will reach livetimes similar to those presented for the feature analysis. The particle sizes where maps yield more X-rays than feature analysis depend on the specific dwelltime and livetime settings, but typically lie in the range between particle areas of 2000 and 15000 pixels, corresponding to equivalent circular diameters of 50 and 140 pixels.

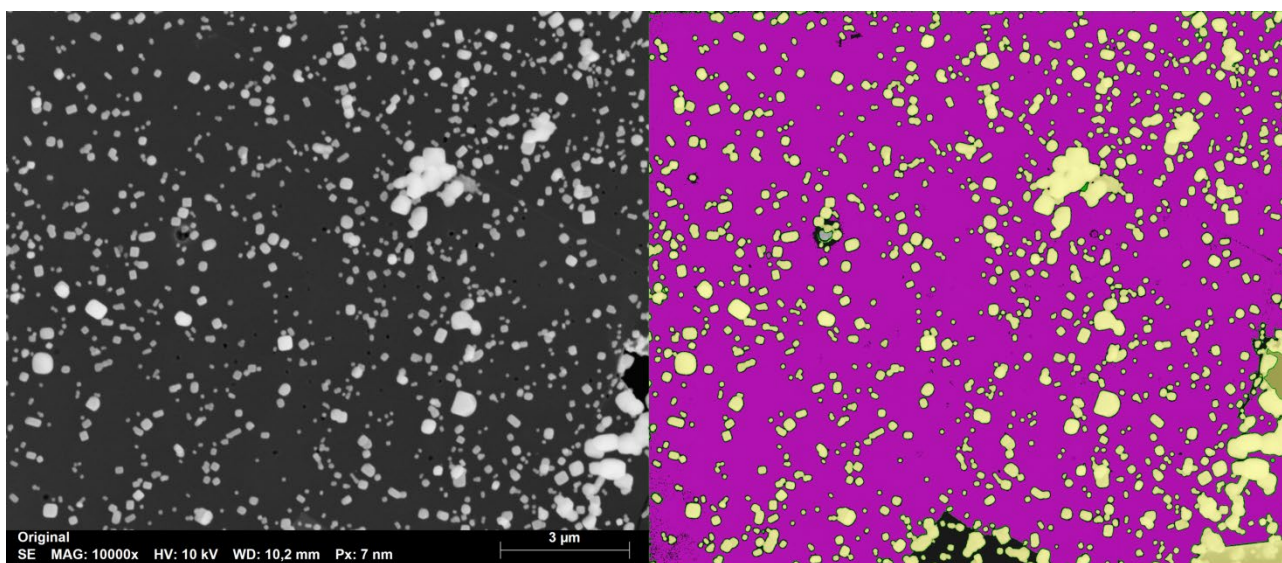
When comparing pixel dwelltimes on the right, it is similarly seen that the pixels in smaller particles are exposed to the electron beam for orders of magnitudes longer when using a fixed particle livetime compared to a fixed dwelltime. As a result, smaller particles are more vulnerable to beam damage for fixed livetimes, as they will be scanned more intensely during the analysis.

Overall there is a trade-off between X-ray yield and risk of beam damage, which should be carefully considered before setting up the analysis. If the composition of small particles is of interest the livetime and minimum X-ray yield settings available with feature analysis can be useful, though they bring an increased risk of beam damage. Alternatively, mapping can be performed at higher

magnification, which will increase the number of pixels in the smaller particles, but will at the same time reduce the sample area covered by the analysis.

### Procedure for background subtraction

When analyzing samples by mapping, it is possible to remove the substrate X-ray contribution from individual particles by segmenting the image into two separate phases, namely a particles phase and a substrate phase, as seen in SI Figure 5. For SE images the particle phase will include all pixels with intensity above a given threshold, while the substrate phase will contain pixels below a given threshold.



SI Figure 7. Left image shows an SE image of the NaCl sample. Right image shows the phase separated SE image, where pixels in the particle phase is yellow, while pixels in the substrate phase are magenta.

Since EDS results are available for all pixels, a spectrum corresponding to the entire substrate phase can be generated and element peak areas identified. By dividing the X-ray counts in each element peak by the area of the substrate phase in pixels, a mean substrate pixel spectrum can be obtained. If it is assumed that the substrate X-ray contribution per pixel is constant, despite it being underneath a particle, the contribution of the substrate can be removed from all particles. Here it is necessary first to scale the mean substrate pixel spectrum to match the size of the particle, by multiplying with the particle area in pixels before subtracting it from the particle spectrum. Once subtracted the X-ray counts can be converted to mass% or at% via Eq. (5). The python code for substrate subtraction used in this paper is available upon request. The code was written to function directly on results obtained with the ESPRIT Software.